The Astrophysical Journal Letters, 989:L7 (18pp), 2025 August 10 https://doi.org/10.3847/2041-8213/ade789

CAPERS-LRD-z9: A Gas-enshrouded Little Red Dot Hosting a Broad-line Active Galactic Nucleus at $z = 9.288$

Anthony J. Taylor[1], Vasily Kokorev[1], Dale D. Kocevski[2], Hollis B. Akins[1], Fergus Cullen[3], Mark Dickinson[4], Steven L. Finkelstein[1], Pablo Arrabal Haro[5,32], Volker Bromm[1], Mauro Giavalisco[6], Kohei Inayoshi[7], Stéphanie Juneau[4], Gene C. K. Leung[8], Pablo G. Pérez-González[9], Rachel S. Somerville[10], Jonathan R. Trump[11], Ricardo O. Amorín[12], Guillermo Barro[13], Denis Burgarella[14], Madisyn Brooks[11], Adam C. Carnall[3], Caitlin M. Casey[15,16], Yingjie Cheng[6], John Chisholm[1], Katherine Chworowsky[1,33], Kelcey Davis[11,34], Callum T. Donnan[4], James S. Dunlop[3], Richard S. Ellis[17], Vital Fernández[18], Seiji Fujimoto[1], Norman A. Grogin[19], Ansh R. Gupta[1,34], Nimish P. Hathi[19], Intae Jung[19], Michaela Hirschmann[20], Jeyhan S. Kartaltepe[21], Anton M. Koekemoer[19], Rebecca L. Larson[19], Ho-Hin Leung[3], Mario Llerena[22], Ray A. Lucas[19], Derek J. McLeod[3], Ross McLure[3], Lorenzo Napolitano[22,23], Casey Papovich[24,25], Thomas M. Stanton[3], Roberta Tripodi[22,26], Xin Wang[27,28,29], Stephen M. Wilkins[30,31], L. Y. Aaron Yung[19], and Jorge A. Zavala[6]

[1] Department of Astronomy, The University of Texas at Austin, Austin, TX, USA; anthony.taylor@austin.utexas.edu
[2] Department of Physics and Astronomy, Colby College, Waterville, ME 04901, USA
[3] Institute for Astronomy, University of Edinburgh, Royal Observatory, Edinburgh EH9 3HJ, UK
[4] NSF's National Optical-Infrared Astronomy Research Laboratory, 950 North Cherry Avenue, Tucson, AZ 85719, USA
[5] Astrophysics Science Division, NASA Goddard Space Flight Center, 8800 Greenbelt Road, Greenbelt, MD 20771, USA
[6] University of Massachusetts Amherst, 710 North Pleasant Street, Amherst, MA 01003-9305, USA
[7] Kavli Institute for Astronomy and Astrophysics, Peking University, Beijing 100871, People's Republic of China
[8] MIT Kavli Institute for Astrophysics and Space Research, 77 Massachusetts Avenue, Cambridge, MA 02139, USA
[9] Centro de Astrobiología (CAB), CSIC-INTA, Ctra. de Ajalvir km 4, Torrejón de Ardoz, E-28850, Madrid, Spain
[10] Center for Computational Astrophysics, Flatiron Institute, 162 5th Avenue, New York, NY 10010, USA
[11] Department of Physics, 196 Auditorium Road, Unit 3046, University of Connecticut, Storrs, CT 06269, USA
[12] Instituto de Astrofísica de Andalucía (CSIC), Apartado 3004, 18080 Granada, Spain
[13] Department of Physics, University of the Pacific, Stockton, CA 90340, USA
[14] Aix Marseille Univ, CNRS, CNES, LAM Marseille, France
[15] Department of Physics, University of California, Santa Barbara, CA 93106, USA
[16] Cosmic Dawn Center (DAWN), Niels Bohr Institute, University of Copenhagen, Jagtvej 128, København N, DK-2200, Denmark
[17] Department of Physics and Astronomy, University College London, Gower Street, London WC1E 6BT, UK
[18] Michigan Institute for Data Science, Unversity of Michigan, 500 Church Street, Ann Arbor, MI 48109, USA
[19] Space Telescope Science Institute, 3700 San Martin Drive, Baltimore, MD 21218, USA
[20] Institute of Physics, Laboratory of Galaxy Evolution, Ecole Polytechnique Federale de Lausanne (EPFL), Observatoire de Sauverny, 1290 Versoix, Switzerland
[21] Laboratory for Multiwavelength Astrophysics, School of Physics and Astronomy, Rochester Institute of Technology, 84 Lomb Memorial Drive, Rochester, NY 14623, USA
[22] INAF—Osservatorio Astronomico di Roma, via Frascati 33, 00078, Monte Porzio Catone, Italy
[23] Dipartimento di Fisica, Università di Roma Sapienza, Città Universitaria di Roma—Sapienza, Piazzale Aldo Moro, 2, 00185, Roma, Italy
[24] Department of Physics and Astronomy, Texas A&M University, College Station, TX, 77843-4242, USA
[25] George P. and Cynthia Woods Mitchell Institute for Fundamental Physics and Astronomy, Texas A&M University, College Station, TX, 77843-4242, USA
[26] IFPU—Institute for Fundamental Physics of the Universe, Via Beirut 2, I-34014 Trieste, Italy
[27] School of Astronomy and Space Science, University of Chinese Academy of Sciences (UCAS), Beijing 100049, People's Republic of China
[28] National Astronomical Observatories, Chinese Academy of Sciences, Beijing 100101, People's Republic of China
[29] Institute for Frontiers in Astronomy and Astrophysics, Beijing Normal University, Beijing 102206, People's Republic of China
[30] Astronomy Centre, University of Sussex, Falmer, Brighton BN1 9QH, UK
[31] Institute of Space Sciences and Astronomy, University of Malta, Msida MSD 2080, Malta
Received 2025 May 9; revised 2025 June 17; accepted 2025 June 23; published 2025 August 6

Abstract

We present CAPERS-LRD-z9, a little red dot (LRD) that we confirm to be a $z = 9.288$ broad-line active galactic nucleus (BLAGN). First identified as a high-redshift LRD candidate from PRIMER NIRCam photometry, follow-up NIRSpec/PRISM spectroscopy of CAPERS-LRD-z9 from the CANDELS-Area Prism Epoch of Reionization Survey (CAPERS) has revealed a broad 3500 km s^{-1} full width at half-maximum Hβ emission line and narrow [O III] $\lambda\lambda$4959, 5007 lines, indicative of a BLAGN. Based on the broad Hβ line, we compute a canonical black hole mass of $\log(M_{\rm BH}/M_{\odot}) = 7.58 \pm 0.15$, although full consideration of systematic uncertainties yields a conservative range of $6.65 < \log(M_{\rm BH}/M_{\odot}) < 8.50$. These observations suggest that either a massive black hole seed or a lighter stellar remnant seed undergoing periods of super-Eddington accretion is necessary to grow such a

[32] NASA Postdoctoral Fellow.
[33] NSF Graduate Fellow.
[34] NSF Graduate Research Fellow.

massive black hole in $\lesssim$500 Myr of cosmic time. CAPERS-LRD-z9 exhibits a strong Balmer break, consistent with a central AGN surrounded by dense ($\sim 10^{10}$ cm^{-3}) neutral gas. We model CAPERS-LRD-z9 using `Cloudy` to fit the emission redward of the Balmer break with a dense-gas-enshrouded AGN and `bagpipes` to fit the rest-ultraviolet emission as a host-galaxy stellar population. This upper limit on the stellar mass of the host galaxy ($<10^9\,M_\odot$) implies that the black hole to stellar mass ratio may be extremely large, possibly >5% (although systematic uncertainties on the black hole mass prevent strong conclusions). However, the shape of the UV continuum differs from typical high-redshift star-forming galaxies, indicating that this UV emission may also be of AGN origin; hence, the true stellar mass of the host may be still lower.

Unified Astronomy Thesaurus concepts: James Webb Space Telescope (2291); Active galactic nuclei (16); AGN host galaxies (2017); Supermassive black holes (1663)

1. Introduction

In the years following its launch, JWST has uncovered previously inaccessible populations of galaxies. These objects include an unprecedented population of galaxies at redshifts of $z > 10$ (e.g., M. Castellano et al. 2022; S. L. Finkelstein et al. 2022; R. P. Naidu et al. 2022; P. Arrabal Haro et al. 2023; B. E. Robertson et al. 2023; B. Wang et al. 2023; S. Carniani et al. 2024; C. T. Donnan et al. 2024; V. Kokorev et al. 2025; J. A. Zavala et al. 2025) and a surprisingly large population of broad-line active galactic nuclei (BLAGN) at $z \gtrsim 6$ (e.g., A. J. Bunker et al. 2023; Y. Harikane et al. 2023; D. D. Kocevski et al. 2023, 2025; V. Kokorev et al. 2023; R. L. Larson et al. 2023; R. Maiolino et al. 2024; H. B. Akins et al. 2024, 2025a; L. J. Furtak et al. 2024; I. Juodžbalis et al. 2024, 2025; J. Matthee et al. 2024; A. J. Taylor et al. 2025; R. Tripodi et al. 2024; B. Wang et al. 2025).

One of the more enigmatic populations identified by JWST is the red compact objects that have been named "little red dots" (LRDs; J. Matthee et al. 2024). These sources were first identified photometrically due to their compact morphology and unique "V-shaped" spectral energy distributions (SEDs), which feature a steep red continuum in the rest-frame optical with relatively blue colors in the rest-frame UV (G. Barro et al. 2024a; D. D. Kocevski et al. 2023; I. Labbé et al. 2023). Subsequent spectroscopic observations have revealed that $\gtrsim$60% of these sources exhibit broad Balmer emission lines that, when coupled with observed narrow forbidden lines, are indicative of BLAGN (D. D. Kocevski et al. 2023, 2025; V. Kokorev et al. 2023; L. J. Furtak et al. 2024; J. E. Greene et al. 2024; J. Matthee et al. 2024). While alternative explanations for these broad-line features have been proposed (e.g., J. F. W. Baggen et al. 2024), several lines of evidence such as high-ionization lines (I. Labbe et al. 2024; R. Tripodi et al. 2024; H. B. Akins et al. 2025a) and Balmer absorption (J. Matthee et al. 2024; X. Ji et al. 2025) point to an AGN powering a significant fraction of the rest-frame optical emission.

LRDs have been shown to be numerous, making up $\sim$20% $-$30% of the BLAGN identified by JWST at $z > 3$ (Y. Harikane et al. 2023; J. E. Greene et al. 2024; R. Maiolino et al. 2024; A. J. Taylor et al. 2025). Their number density matches or exceeds the total pre-JWST expected contribution of UV-faint ($M_{\rm UV} > -21$) AGN to the UV luminosity function at $4.5 < z < 8.5$, and LRDs represent $\sim$1% of the total galaxy UVLF over the same range (S. L. Finkelstein & M. B. Bagley 2022; V. Kokorev et al. 2024a; A. J. Taylor et al. 2025; D. D. Kocevski et al. 2025). Under the BLAGN interpretation, LRDs host supermassive black holes (SMBHs), with some reaching $M_{\rm BH} > 10^7\,M_\odot$ within the first Gyr of cosmic time. These objects thus provide insight into black hole seeding and growth in the early Universe (e.g., A. Smith & V. Bromm 2019; T. E. Woods et al. 2019; K. Inayoshi et al. 2020; J. Regan & M. Volonteri 2024; J. Jeon et al. 2025a).

However, analysis of the rest-frame near-infrared (near-IR) or observed mid-infrared (mid-IR) emission of LRDs further complicates their physical interpretation. Observations with JWST/MIRI have shown a surprisingly flat continuum at rest-frame 1–3 μm (e.g., H. B. Akins et al. 2024; G. Barro et al. 2024b; G. C. K. Leung et al. 2024; P. G. Pérez-González et al. 2024; C. C. Williams et al. 2024), suggesting a lack of a hot dusty torus commonly seen in reddened AGN at up to $z \sim 6$ (e.g., R. Barvainis 1987; J. Lyu & G. Rieke 2022). Full SED analysis using NIRCam and MIRI shows either no correlation (G. C. K. Leung et al. 2024) or a negative correlation (G. Barro et al. 2024b) between the apparent extinction in LRDs and their rest-MIR emission, indicating an alternative source of obscuration than hot dust. Moreover, applying a conventional AGN SED model with dust obscuration implies highly overmassive black holes in LRDs, hinting at either some stellar contribution or super-Eddington accretion (G. C. K. Leung et al. 2024).

A subset of LRDs with deep JWST/NIRSpec PRISM spectroscopy exhibit strong Balmer breaks (e.g., D. J. Setton et al. 2024; B. Wang et al. 2024). While this initially suggested that the emission at these wavelengths must be dominated by stars, some of these objects exhibit greater break strengths than are possible from an evolved stellar population alone (e.g., I. Labbe et al. 2024; C. C. Williams et al. 2024; A. de Graaff et al. 2025; X. Ji et al. 2025; R. P. Naidu et al. 2025), thus requiring an alternative explanation. K. Inayoshi & R. Maiolino (2025) suggest that generating such breaks is in fact possible without stellar emission by instead modeling an AGN enshrouded by a cocoon of dense neutral gas. In this model, the high column density of this gas results in a significant population of $n = 2$ collisionally excited-state hydrogen atoms that resonantly scatter Balmer line emission and absorb and reprocess light at wavelengths less than the Balmer limit ($\sim$3650 Å), much like photons blueward of the Lyman limit in less-dense gas where the bulk of hydrogen atoms are in the ground state. This results in a stronger Balmer break and narrow absorption features superimposed upon the broad Balmer emission lines. These absorption features have indeed been identified in several LRDs (J. Matthee et al. 2024; A. J. Taylor et al. 2025; B. Wang et al. 2025; A. de Graaff et al. 2025; X. Ji et al. 2025; D. D. Kocevski et al. 2025; R. P. Naidu et al. 2025; V. Rusakov et al. 2025). This theory also helps explain the lack of X-ray emission exhibited by LRDs due to Compton-thick absorption (M. Yue et al. 2024a; D. D. Kocevski et al. 2025; R. Maiolino et al. 2025) as well as the higher Balmer

decrements observed from broad lines compared to narrow lines (e.g., M. Brooks et al. 2025; R. P. Naidu et al. 2025).

The origin and growth histories of these SMBHs remain an open puzzle (K. Inayoshi et al. 2020; M. Volonteri et al. 2021). The most commonly considered scenarios for creating seed black holes can be divided into two categories: (1) light seeds ($m_{\rm seed} \sim 100\ M_\odot$), left behind as stellar remnants of massive Population III stars, and (2) heavy seeds, which may form via runaway collisions in dense environments such as stellar clusters (thought to create seeds with $m_{\rm seed} \sim 10^3$–$10^4\ M_\odot$, which may rapidly grow to $\sim 10^5$–$10^6\ M_\odot$ via mergers) or via direct collapse of primordial gas clouds under special conditions such as strong Lyman–Werner radiation fields, high baryon-dark matter streaming velocity, or gas-rich mergers, leading to seeds with masses $m_{\rm seed} \sim 10^5$–$10^6\ M_\odot$ (see review by K. Inayoshi et al. 2020 and references therein). A more exotic origin for seed BHs, involving a qualitatively different evolutionary sequence, is primordial black holes that form shortly after the Big Bang (e.g., B. Liu & V. Bromm 2022; A. Matteri et al. 2025; S. Zhang et al. 2025; F. Ziparo et al. 2025). It is possible, even likely, that multiple mechanisms contribute to seeding the black hole population that we observe.

In order to reach the masses of the detected high-redshift black holes, light seeds must grow at or above the Eddington rate with a high duty cycle from an early epoch ($z \gtrsim 20$). Heavier seeds can grow at more moderate rates. For the broader category of non-LRD broad-line high-redshift AGN, the estimated black hole masses appear to make many of these objects "overmassive" compared to their stellar hosts, with black hole to stellar mass ratios far above the typical $M_{\rm BH}/M_* \sim 0.1\%$ exhibited by local dormant black holes and AGN (B. Agarwal et al. 2013; F. Pacucci et al. 2023). However, we note that analyzing this "overmassiveness" on a population level may be subject to Lauer bias (the tendency to observe a greater number of massive black holes as outliers in intrinsically common moderate-mass galaxies, rather than in intrinsically rarer high-mass galaxies; T. R. Lauer et al. 2007; J. Li et al. 2025). The stellar masses of LRDs are particularly uncertain, given that it is unknown whether the observed UV light comes from the AGN or the stars, but some estimates suggest that they may have some of the most extreme overmassive BHs, with some approaching $\sim$10%–100% of the host galaxy's stellar mass (e.g., V. Kokorev et al. 2023; R. Maiolino et al. 2024; C.-H. Chen et al. 2025; D. D. Kocevski et al. 2025). Heavy seeds would provide one obvious explanation for overmassive black holes, but there are other explanations, such as periods of more rapid growth of the black hole relative to the stars, or selection effects. Pushing black hole detections to earlier cosmic epochs, closer to the presumed epoch of black hole seeding, is one of the most promising avenues to disentangle the degeneracies between seeding and accretion physics.

These numerous open questions have prompted ongoing campaigns for spectroscopic follow-up of photometrically identified LRDs, especially those at high photometric redshifts ($z \gtrsim 9$). Here, we present CAPERS-LRD-z9, the highest-redshift spectroscopically confirmed LRD and BLAGN yet discovered. The source was first identified as a high-z LRD candidate in D. D. Kocevski et al. (2025) and subsequently also selected by G. Barro et al. (2024b) and H. B. Akins et al. (2024). It was also independently selected as a galaxy candidate at $z = 9$–10 by C. T. Donnan et al. (2024). We now observe this source using NIRSpec observations taken as part of the CANDELS-Area Prism Epoch of Reionization Survey (CAPERS) program (GO-6368; PI: M. Dickinson).

This Letter is organized as follows. First, in Section 2, we describe the JWST NIRCam, NIRSpec, and MIRI data used in the discovery and follow-up of CAPERS-LRD-z9. In Section 3, we describe our measurements of the spectroscopic redshift, emission line properties, morphology, Balmer decrement, and Balmer break in CAPERS-LRD-z9. In Section 4, we compute the black hole and stellar masses of CAPERS-LRD-z9, and we discuss the implications of these properties and the applicability of the dense neutral gas model of LRDs to this source. Finally, we summarize our work in Section 6. We assume a flat Lambda cold dark matter cosmology with $\Omega_m = 0.3$, $\Omega_\Lambda = 0.7$, and $H_0 = 70\ {\rm km\ s^{-1}\ Mpc^{-1}}$ throughout. All magnitudes are given in the AB magnitude system (J. B. Oke & J. E. Gunn 1983), where an AB magnitude is defined by $m_{\rm AB} = -2.5 \log f_\nu - 48.60$. Here, f_ν is the specific flux density of the source in units of erg cm^{-2} s^{-1} Hz^{-1}.

2. Observations and Data Reduction

CAPERS-LRD-z9 was first identified as a potential very high-redshift LRD from the JWST NIRCam imaging provided by the Public Release IMaging for Extragalactic Research (PRIMER) survey (J. S. Dunlop et al. 2021) in the COSMOS field (H. B. Akins et al. 2024; G. Barro et al. 2024b; D. D. Kocevski et al. 2025). The LRD selection was based on an analysis of the rest-frame UV and optical SED slopes following determination of the source's photometric redshift with EAZY (G. B. Brammer et al. 2008). As potentially the highest-redshift LRD discovered to date, CAPERS-LRD-z9 was identified as a high-value target for CAPERS; therefore, it was selected to receive a slitlet and a full-depth CAPERS integration (see Section 2.1). While the full details of the CAPERS target selection, data reduction, and program design will be described in future works, we summarize the observations below.

2.1. NIRSpec Observations

CAPERS is a JWST Cycle 3 legacy program that uses NIRSpec/Micro-shutter Assembly (MSA)/PRISM to observe very high-redshift galaxies, AGN candidates, and other objects of community interest in three of the CANDELS legacy fields (N. A. Grogin et al. 2011; A. M. Koekemoer et al. 2011) as identified from the deep multiband NIRCam imaging provided by the PRIMER (J. S. Dunlop et al., in preparation) and Cosmic Evolution Early Release Science (S. L. Finkelstein et al. 2025) JWST surveys.

CAPERS is targeting seven MSA pointings in each of the PRIMER-UDS, PRIMER-COSMOS, and extended Groth strip fields, observing three MSA configurations at each pointing. This multiconfiguration approach allows CAPERS to observe high-value targets in multiple configurations to increase their exposure times while simultaneously observing a large number of other targets in each individual configuration to increase the overall sample yield. As a high-value target, CAPERS-LRD-z9 (aka CAPERS-COSMOS-119334) was observed in all three configurations executed in CAPERS COSMOS pointing P4. These observations targeting CAPERS-LRD-z9 were executed on 2025 April 15 using two iterations of a standard three-

shutter nodding scheme per MSA configuration for a total of 18 exposures at a NIRSpec aperture position angle (east of north) of 246.°585. Each of these 18 nods was observed for a single 13 group integration using the NRSIRS2 readout pattern for a combined effective exposure time of 17,069 s (4.74 hr).

We reduced the spectroscopic data using the JWST Calibration Pipeline[35] (H. Bushouse et al. 2025) version 1.17.1 and CRDS version 1350.pmap. We largely used the default configuration for the pipeline, with a few notable exceptions. First, we enabled the clean_flicker_noise step (using the "median" method[36]) in the calwebb_detector1 stage to remove the effects of $1/f$ noise in the count rate maps. We also employed a modified flat-field file in the calwebb_spec2 stage (see P. Arrabal Haro et al. 2023 for details). Beyond these changes, we ran the calwebb_spec3 stage using the CRDS defaults to produce a final 2D spectrum (see Figure 1, bottom panel).

We next used a custom optimal extraction (K. Horne 1986) to best detect and extract the signal from the source in the 2D spectrum to produce a 1D spectrum. Finally, we calibrated this 1D spectrum to the JWST/NIRCam photometry provided by the PRIMER survey (Section 2.2) by computing the total flux in the spectrum within each of the F150W, F200W, F277W, F356W, and F444W NIRCam passbands. Specifically, we compared these measured fluxes to the photometric measurements of the object from NIRCam and fitted a third-order Chebyshev polynomial to the ratios between the spectrum and the photometry (as in bagpipes; A. C. Carnall et al. 2018). This correction peaks at a factor of ∼0.9 in F150W and quickly flattens to ∼0.7 from F200W through F444W. We then multiplied the 1D spectrum by the resulting fitted correction curve to produce our final calibrated 1D spectrum (see Figure 1, bottom panel). This calibration is necessary to correct for the effects of NIRSpec path loss and automated corrections applied in the JWST Calibration Pipeline that are not tied to NIRCam data.

2.2. NIRCam Photometry

The analysis in this Letter makes use of JWST/NIRCam photometry in the PRIMER-COSMOS field. This imaging is an internal reduction from the PRIMER team (internal version 1.0). The PRIMER imaging data were reduced using the PRIMER Enhanced NIRCam Image Processing Library (J. S. Dunlop et al. 2025, in preparation; D. Magee et al. 2025, in preparation) software.

The photometry was measured via a similar process as in S. L. Finkelstein et al. (2024). Briefly, for each band of imaging, this methodology point-spread function (PSF) matches images (using empirical PSFs) with smaller PSFs than F277W to that band and derives correction factors for images with larger PSFs (via PSF-matching F277W to a given larger PSF). Kron apertures are used to measure colors to optimize the signal-to-noise for high-redshift galaxies. Total fluxes are estimated by deriving an aperture correction in the F277W band as the ratio between the flux in the larger Kron aperture and the custom smaller aperture, with a residual aperture correction (typically <10%) derived via source-injection simulations. We show cutouts of the imaging of CAPERS-LRD-z9 and list the measured magnitudes in Figure 1 (top panel).

2.3. MIRI Photometry

We searched the Barbara A. Mikulski Archive for Space Telescopes (MAST) for MIRI data at the position of CAPERS-LRD-z9. They were located in a gap of the PRIMER observations but were covered by the COSMOS-3D survey (PID 5893) on 2025 April 20. Raw data were downloaded from MAST and reduced with the Rainbow MIRI software (P. G. Pérez-González et al. 2024) using the JWST Calibration Pipeline version v1.18.0, reference files in jwst_1364.pmap. The Rainbow software implements a superbackground strategy to remove and homogenize the background, improving the detectability of faint sources. We refer the reader to P. G. Pérez-González et al. (2024) and G. Östlin et al. (2025) for details on the method and a discussion of improvements compared to exposure time calculator estimations. COSMOS-3D obtained data in the F1000W and F2100W filters, with exposure times of 927 s and 1848 s, respectively. The average 5σ detection limits for pointlike sources measured in a circular aperture of radius $r = 0.''3$ and $0.''7$ for F1000W and F2100W are 24.8 and 22.8 mag, respectively (calculated with the method described below).

We measured photometry in the two MIRI bands assuming a pointlike nature and applying aperture corrections based on the empirical PSFs provided by the JWST Calibration Pipeline. We used several circular apertures in each band. We selected radii ranging from $0.''2$ to $0.''5$ for F1000W and $0.''4$ to $1.''0$ for F2100W, the ranges of aperture sizes chosen to be able to detect faint sources and limited to maximum/minimum aperture losses of 50%/25% for pointlike sources. The background was measured in a $r = 10''$ circular region around the source. For the background noise (used to get photometric uncertainties and the 5σ detection limits quoted above), following the method explained in P. G. Pérez-González et al. (2023; based on P. G. Pérez-González et al. 2008), we selected random noncontiguous pixels (separated by more than 3 pixels) to avoid the effects of noise correlation (i.e., an underestimation of the rms) introduced by the drizzling method when mosaicking the data.

For F1000W, we obtained consistent photometric measurements (within the errors) with all apertures, the measurements ranging from 24.90 ± 0.29 mag for $r = 0.''2$ to 25.63 ± 0.59 mag for $r = 0.''5$. The final magnitude used in the rest of the Letter, the one with the maximum S/N obtained with $r = 0.''3$ (aperture correction 0.60 ± 0.03 mag, the errors accounting for a 1 pixel centering error), is 25.02 ± 0.26 mag.

For F2100W, we obtained negative fluxes or S/N < 2 measurements for all apertures, so we conclude that there is a nondetection in this band and assume the 5σ upper limit quoted above of 22.8 mag (corresponding to an aperture of radius $r = 0.''9$, where the encircled energy is ∼70%).

3. Data Analysis

3.1. Spectroscopic Redshift

The CAPERS team is using a combination of software tools, interactive inspection, and manual vetting to measure redshifts from the NIRSpec spectra; the full methodology will be detailed in a forthcoming publication. For CAPERS-LRD-z9, we derive the initial spectroscopic redshift using a modified

[35] https://github.com/spacetelescope/jwst

[36] Based on image1overf.py, https://github.com/chriswillott/jwst.

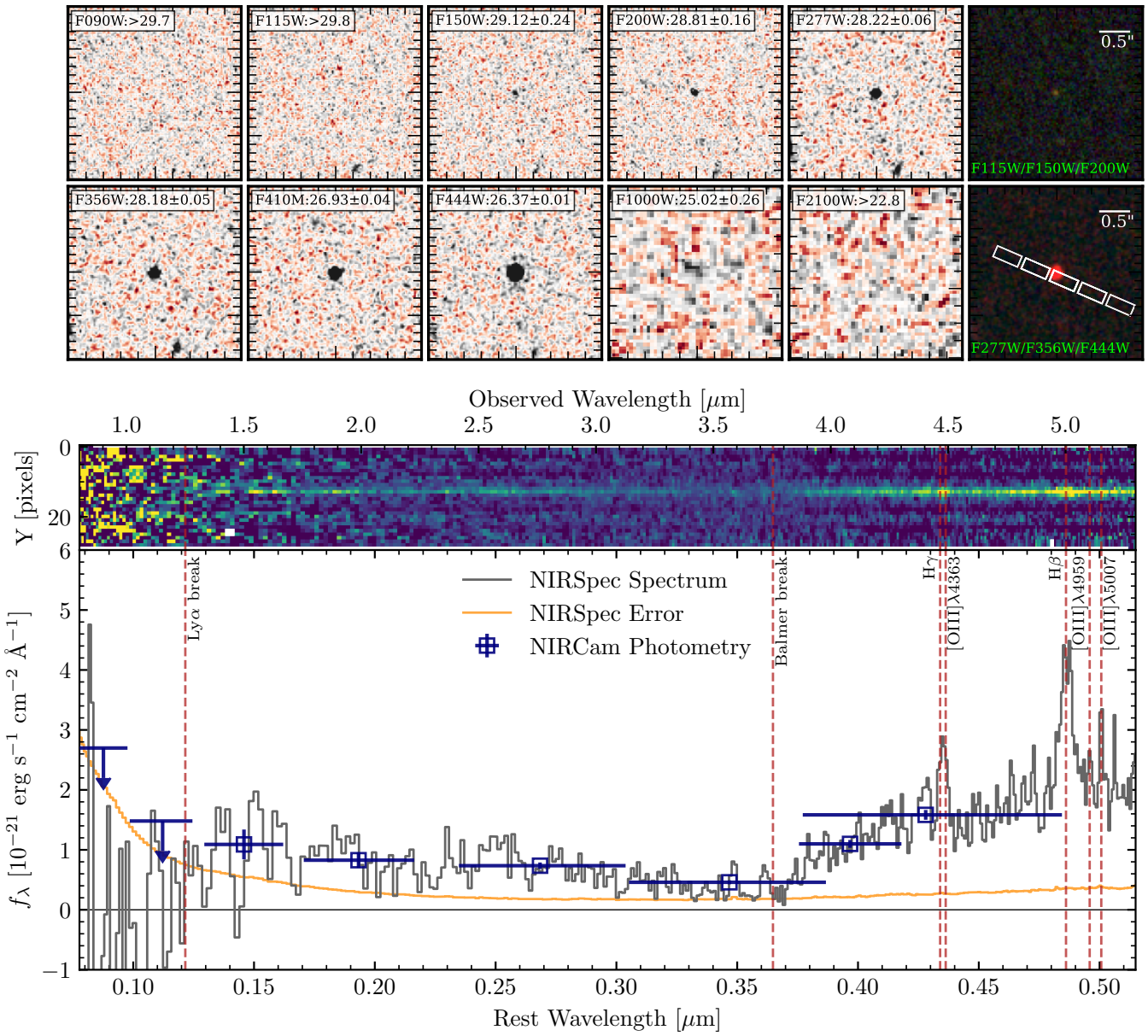

Figure 1. Top: $5'' \times 5''$ NIRCam and MIRI cutouts of CAPERS-LRD-z9 in the PRIMER-COSMOS NIRCam and COSMOS-3D MIRI images. We also show RGB images generated for both the short-wavelength and long-wavelength NIRCam detectors. We overplot the NIRSpec MSA slitlet. Bottom: we plot the 2D and 1D photometrically calibrated spectra of CAPERS-LRD-z9 in f_λ. We mark strongly detected emission features with red dashed lines and overplot the NIRCam photometry with blue squares. Despite being near the corner of the central shutter in the slitlet, CAPERS-LRD-z9 exhibits a detectable Lyα break, a strong Balmer break, and clear rest-optical emission line detections, including broadened Hβ and Hγ and narrow [O III] $\lambda\lambda$4959, 5007. The combination of narrow forbidden lines and a broad Hβ clearly indicates that CAPERS-LRD-z9 is a BLAGN at $z = 9.288$.

version of `msaexp`[37] (G. Brammer 2022; V. Kokorev et al. 2024b). Key modifications include the ability to vary the velocity width and model individual lines with multiple components (e.g., narrow and broad).

We use `msaexp` to fit the continuum with cubic splines and emission lines with Gaussian profiles. For this step, we adopt `nsplines = 20`, leaving the position, amplitude, and width of the emission lines as free parameters. The full width at half-maximum (FWHM) is allowed to vary between 150 and 800 km s^{-1} for narrow components and 800 and 5000 km s^{-1} for broad ones. Uncertainties are estimated via Markov Chain Monte Carlo (MCMC) using resampling of the covariance matrix. All fits are performed on spectra corrected to match the photometry. To account for the wavelength-dependent resolution of PRISM, the model grid is initially generated on an oversampled wavelength axis and then convolved with the instrument dispersion curve.

With this automated multiline fitting approach, we derive an initial $z_{\rm spec} = 9.2880 \pm 0.065$ and a number of interesting features. Broad components in excess of $\sim$3000 km s^{-1} (FWHM) are required to adequately model both the Hγ and Hβ emission, while the adjacent lines in the [O III] $\lambda\lambda$4959, 5007 doublet remain narrow ($\sim$200 km s^{-1} FWHM). The presence of broad permitted (e.g., Balmer series of hydrogen) and narrower (semi)forbidden lines like [O III] gives us a first hint that an accreting SMBH is present in CAPERS-

[37] https://github.com/VasilyKokorev/msaexp_OLF

LRD-z9, typical of other spectroscopic investigations of LRDs with JWST (e.g., J. Matthee et al. 2024; A. J. Taylor et al. 2025; D. D. Kocevski et al. 2025).

We note that this redshift fitting routine is not always capable of accurately modeling all spectral features. While it performs well for most narrow and broad emission lines and is efficient for processing large spectral samples, its reliability decreases in the presence of complex line blends, uncommon line ratios, low signal-to-noise regions, or noisy continua. Accurate identification of key features, such as broad lines, is essential for robust classification of the object, especially when using the PRISM data. Therefore, in subsequent sections, we adopt a more refined fitting procedure for select regions of the spectrum.

3.2. Line Fitting

The spectrum of our object presented in Figure 1 coupled with our initial `msaexp` fit hints at the presence of broad components in both Hγ and Hβ emission lines, in contrast to the narrower profiles of the adjacent [O III] $\lambda\lambda$4959, 5007 Å doublet. Further, the Hβ line appears to be double-peaked, which hints at an underlying absorption component. To evaluate the potential significance of these features, we perform a more detailed line fitting to the Hγ + [O III] λ4363 and Hβ + [O III] $\lambda\lambda$4959, 5007 line complexes. The redder end of PRISM, where Hβ + [O III] $\lambda\lambda$4959, 5007 is located, has a higher spectral resolution, and this line complex is not blended; therefore, we fit that region first. We assume that the lines in the [O III] doublet are both narrow, while the Hβ consists of a narrow, a broad, and an absorption component. In our fitting, we assume that the velocity width of the narrow component for all three lines is the same, and we fix the ratio [O III] λ5007/[O III] λ4959 = 2.98 (P. J. Storey & C. J. Zeippen 2000). Velocities of the narrow, broad, and absorption components are allowed to vary between 50 and 800, 1000 and 5000, and 50 and 1000 km s^{-1}, respectively. We fix the redshift (and thus the line centers of the narrow lines using the vacuum wavelengths from P. A. M. van Hoof 2018); however, we allow for small ($\sim\pm$500 km s^{-1}) offsets in the absorption component and broad component of Hβ (relative to the narrow [O III]) to allow for kinematic motion of the gas. We model the local continuum with a first-order polynomial.

We initialize the fit by first creating a set of models on the oversampled wavelength grid. To mimic the variable resolution of PRISM, we interpolate our model onto a variable step grid while making sure that the total integrated flux is preserved. Early NIRSpec/MSA results (A. G. de Graaff et al. 2023) have shown that the spectral resolution of a pointlike source falling within a slitlet is higher compared to a uniformly illuminated slit, sometimes up to a factor of 2. We therefore conservatively increase the nominal spectral resolution by a factor of 1.7. To take into account the effects of the line-spread function, we additionally convolve our model with Gaussians of variable resolution (A. G. de Graaff et al. 2023; Y. Isobe et al. 2023). We then optimize this fit via MCMC with the `emcee` (D. Foreman-Mackey et al. 2013) package for `python`.

From our fit, we securely (combined S/N $\approx$ 4.2) confirm the presence of the [O III] $\lambda\lambda$4959, 5007 doublet at a redshift $z = 9.288 \pm 0.003$. We adopt this redshift for all subsequent calculations. We also detect a distinct broad component in Hβ at S/N $\approx$ 10, with an intrinsic FWHM = 3521 $\pm$ 502 km s^{-1} and a tenuous slight redward velocity offset from the systemic redshift of 134 $\pm$ 164 km s^{-1}. The width of the narrow lines is poorly constrained due to the low resolution of PRISM, although we report a posterior value of FWHM = 483 $\pm$ 225 km s^{-1}. The narrow component of Hβ does not appear to be statistically significant (S/N $\approx$ 0.8). Additionally, while including the Hβ absorption component results in a visually better fit to the double-peaked $H\beta$ line with a line width of FWHM = 413 $\pm$ 255 km s^{-1} and slight redward offset of 84 $\pm$ 126 km s^{-1}, this component is also statistically insignificant with S/N $\approx$ 1.1 and highly degenerate with the narrow Hβ component. These statistical nondetections may be expected at the resolution of PRISM, but as they are physically motivated, we include them in the model regardless to better sample their covariance with the more significant model components.

The situation with Hγ + [O III] λ4363 is more complex, as these lines are blended at the PRISM resolution. We can, however, use the prior information obtained from the Hβ + [O III] $\lambda\lambda$4959, 5007 complex and attempt to adequately separate the two lines. We fix the narrow and broad line widths, broad velocity offset, and redshift to the result we obtained from the Hβ + [O III] $\lambda\lambda$4959, 5007 fit and only fit the integrated fluxes of narrow+broad Hγ, narrow [O III] λ4363, and a first-order polynomial continuum. Finally, the flux ratio of the narrow Hγ to narrow Hβ is not allowed to exceed 0.47, as set by Case B recombination (D. E. Osterbrock 1989). This fit is further complicated by 6 consecutive pixels at 4.375–4.425 μm that show flux above the level of the nearby continuum. While these pixels are detected at the 1σ–3σ level above the continuum, they correspond to no known emission line. Therefore, we conservatively mask out this spurious feature. We once again forward model the effects of the PRISM resolution and fit the Hγ + [O III] λ4363 line complex with MCMC. Similarly to Hβ, we could not derive a significant flux for a narrow Hγ (S/N $\approx$ 2); however, we detect and partially deblend a broad Hγ component at S/N $\approx$ 4.8 and [O III] λ4363 at S/N $\approx$ 3.1. We note that the blue wing of the broad Hγ line appears higher than the data. This may indicate that the masked spurious feature is affecting these pixels or that the Hγ broad line width is narrower than that of Hβ, as has been seen in low-redshift quasars (e.g., M. C. Bentz et al. 2023). As our analyses are not dependent on the Hγ width, this uncertainty does not affect our interpretation of this object. We present various measured and derived properties of CAPERS-LRD-z9 in Table 1 and show our best-fit models to both line complexes in Figure 2.

3.3. Morphology and Size Measurements

To determine if any of the emission from CAPERS-LRD-z9 might originate from an extended stellar population, we use the `GALFIT` software (C. Y. Peng et al. 2002) to model the galaxy as a point source in several NIRCam bands to search for signs of an underlying galaxy in the residual image. For this modeling, we provide `GALFIT` with empirical PSFs constructed from the PRIMER-COSMOS mosaic and noise images that account for both the intrinsic image noise (e.g., background and readout noise) and added Poisson noise due to the objects themselves. We show the results of this morphological modeling in Figure 3 for F200W and F444W. We see no signs of any extended structure, indicating that the

Table 1
Properties of CAPERS-LRD-z9

Property	Value
R.A.	150.1362532
Decl.	2.3080298
Redshift (z)	9.288 ± 0.003
Hγ flux (narrow)	<7.1
Hγ flux (broad)	45.9 ± 9.5
[O III] λ4363 flux	13.0 ± 4.2
Hβ flux (narrow)	<62.7
Hβ flux (broad)	140 ± 14.6
Hβ flux (absorption)	>-69.1
$H\beta_{broad}$ FWHM	3521 ± 502 km s^{-1}
$H\beta_{abs}$ FWHM	282 ± 159 km s^{-1}
$H\beta_{broad}$ offset	134 ± 164 km s^{-1}
$H\beta_{abs}$ offset	84 ± 126 km s^{-1}
[O III] λ4959 flux	7.2 ± 3.5
[O III] λ5007 flux	22.2 ± 5.3
[O III] λ5007 FWHM	483 ± 225 km s^{-1}
$M_{1500\ Å}$	-18.2 ± 0.2 mag
β_{UV}	$-0.99^{+0.14}_{-0.13}$
$\log(M_{BH}/M_\odot)$ (canonical)	7.58 ± 0.15
$\log(M_{BH}/M_\odot)$ (systematic bounds)	6.65–8.50
$A_{V,BLR}$	$1.9^{+1.3}_{-1.2}$
$\log(M_*/M_\odot)$	<9.0
M_{BH}/M_* (canonical)	>4.5%
M_{BH}/M_* (systematic bounds)	>46%, >0.5%
Balmer break: ($f_{\nu,4050\ Å}/f_{\nu,3670\ Å}$)	$4.35^{+0.93}_{-0.67}$

Note. All line fluxes are given in units of 10^{-20} erg s^{-1} cm^{-2}. Lines fit at S/N $\leqslant 2$ are listed as 2σ (upper/lower) limits on their fluxes. We define a "canonical" $\log(M_{BH}/M_\odot)$ and uncertainties as only those errors propagating from the measured broad-line properties and the empirical uncertainties given in J. E. Greene & L. C. Ho (2005) without correcting for dust. We further provide upper and lower bounds on $\log(M_{BH}/M_\odot)$ to account for systematic uncertainties in the measurement methods (see Section 4.2 for details).

source is unresolved or the surface brightness of the resolved component is too low for detection with the sensitivity of our image. We estimate an upper limit on the size of the host to be $r_h < 0.''04$ and $0.''08$ in F200W and F444W, respectively, which correspond to physical sizes of $\lesssim$175 pc and $\lesssim$350 pc.

3.4. Spectrophotometric Fitting

We model the SED of CAPERS-LRD-z9 as a composite galaxy+AGN, similar to previous work on LRDs with Balmer breaks (e.g., I. Labbe et al. 2024; B. Wang et al. 2024). However, here we model the Balmer break as part of the AGN continuum (rather than old stars), driven by absorption from a shell of dense gas around the accretion disk/broad-line region (BLR; e.g., K. Inayoshi & R. Maiolino 2025; X. Ji et al. 2025; R. P. Naidu et al. 2025). We explored modeling the spectrum using only a stellar component, with a flexible nonparametric star formation history (SFH) driving the strong Balmer break with an old stellar population (>300 Myr). Comparing the fluxes on either side of the break (in 100 Å wide windows centered at 3670 and 4050 Å), our best-fit stellar-only model has a break strength of ~2.8. This is insufficient to match the strength of the break in CAPERS-LRD-z9 (which we measure as $f_{\nu,4050\ Å}/f_{\nu,3670\ Å} = 4.35^{+0.93}_{-0.67}$), similar to other recently discovered LRDs with extreme Balmer breaks (RUBIES-BLAGN-1, $2.73^{+0.20}_{-0.17}$, B. Wang et al. 2025; A2744-QSO1, $3.33^{+0.15}_{-0.15}$, Y. Ma et al. 2025, A. Weibel et al. 2025; MoM-BH*-1, $7.7^{+2.3}_{-1.4}$, R. P. Naidu et al. 2025; RUBIES-UDS-154183, $6.9^{+2.8}_{-1.5}$, A. de Graaff et al. 2025). The stellar-only model is overall a poor fit to the data, with a Bayesian information criterion (BIC) difference from our fiducial model (described below) of ΔBIC > 80. This, combined with the significant detection of broad Hβ, drives our assumption that the rest-frame optical is dominated by the AGN, enshrouded in dense gas.

We therefore pursue a more complex modeling, first using the `Cloudy` photoionization code (version 23.01; M. Chatzikos et al. 2023) to generate a large grid of AGN model SEDs, varying both the intrinsic AGN accretion disk SED and the gas conditions around the source. We follow the framework described in K. Inayoshi & R. Maiolino (2025) and R. P. Naidu et al. (2025) and model the intrinsic AGN accretion disk SED as a series of power laws combined with a "big bump" temperature.[38] This continuum is passed through a shell of gas surrounding the central source that is defined in terms of its density, metallicity, and turbulent velocity. The turbulence is required to reproduce the break shape; without it, the break is very sharp at $\lambda = 3650$ Å. We vary the ionization parameter that sets the ratio of H-ionizing photons to gas densities at the illuminated face of the gas cloud. When all other parameters are fixed, varying the ionization parameter is equivalent to varying the distance between the central source and the gas shell. We stop the calculation at a set of fixed line-of-sight column densities through the gas cloud. The full grid of `Cloudy` model parameters is provided in Table 2.

In order to conduct joint inference on the AGN and galaxy parameters, we assemble and fit the full SED model using a modified version of `bagpipes` (A. C. Carnall et al. 2018), a Bayesian SED modeling code. `bagpipes` requires models with a continuous parameter space, rather than discrete points in a grid; we include a custom module to interpolate over the `Cloudy` grid (consisting of both the continuum and emission lines of the AGN processed through the dense gas shell).

However, in an effort to reduce the dimensionality of the problem, prior to fitting with `bagpipes`, we first perform a simple χ^2 minimization routine over the `Cloudy` grid to identify and fix the best-fit values of several grid parameters. Here, we fit only to the PRISM spectrum redward of the Balmer break and include several postprocessing steps, including broadening of the AGN emission lines, a variable covering fraction of the BLR clouds, and dust attenuation following a Small Magellanic Cloud (SMC) law (K. D. Gordon et al. 2003). Fitting to our grid, we find that the best-fit model has $\log T_{BB}/\mathrm{K} = 5$, $\alpha_{OX} = -1.5$, $\log n_H/\mathrm{cm}^{-3} = 9.5$, $v_{turb} = 100$ km s^{-1}, $\log U = -1.5$, and $\log N_H/\mathrm{cm}^{-2} = 26$. We note that these parameters describe a Compton-thick environment that `Cloudy` is not designed to simulate.[39] Therefore, while we caution that our `Cloudy` models may not capture all physical processes in this regime, `Cloudy` remains the best accessible tool for this modeling.

In the subsequent modified `bagpipes` fit, we then fix T_{BB}, α_{OX}, and $\log U$ at their best-fit values and interpolate over the density $\log n_H$, column density $\log N_H$, and turbulent velocity

[38] This AGN continuum model is described in Section 6.2 of the HAZY1 `Cloudy` documentation (version 23.01).
[39] See Section 3.4 of the HAZY2 `Cloudy` documentation.

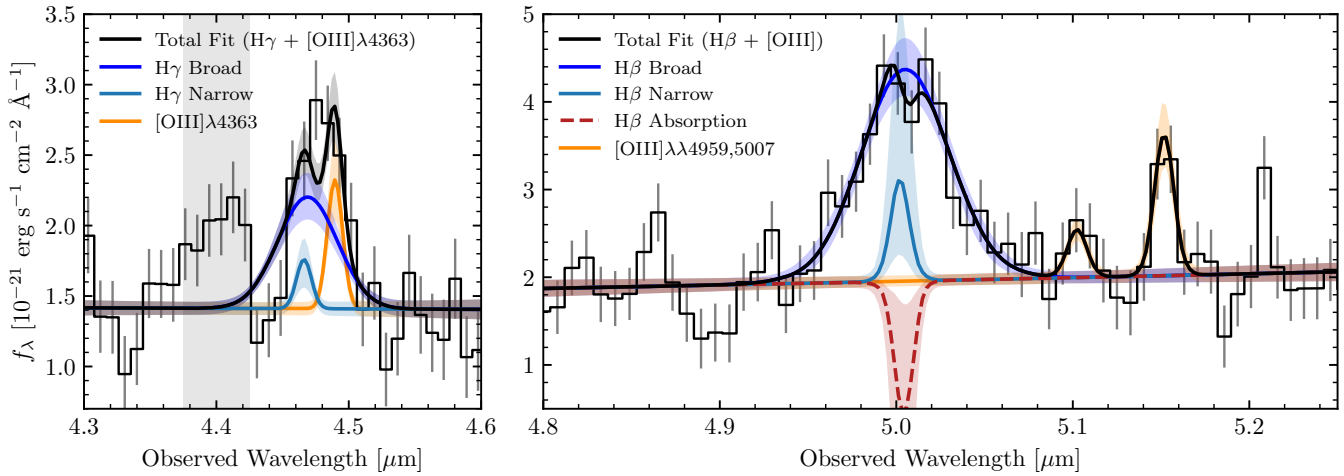

Figure 2. The observed NIRSpec/PRISM spectrum of CAPERS-LRD-z9 is shown as the fine black curve with uncertainties in gray. Left: line fits and 1σ uncertainties on Hγ (blue curves and shaded regions), [O III] λ4363 (orange curve and shaded region), and the combined fit (thick black curve and shaded region). We deblend these lines using the high-confidence line widths and redshift solution measured from Hβ + [O III] $\lambda\lambda$4959, 5007. We show the region of masked spurious pixels with gray shading. Right: line fits to Hβ + [O III] $\lambda\lambda$4959, 5007. A broad (FWHM = 3521 $\pm$ 502 km s^{-1}; blue curve) component is clearly necessary to reproduce the Hβ. We also fit narrow emission (light blue) and absorption (dashed red) components to Hβ to better model the double-peak structure of the line, though their fluxes are degenerate at PRISM resolution. The [O III] $\lambda\lambda$4959, 5007 doublet is also detected at S/N $\sim$ 4. The combination of narrow [O III] $\lambda\lambda$4959, 5007 and broad Hβ is a clear indicator of a BLAGN.

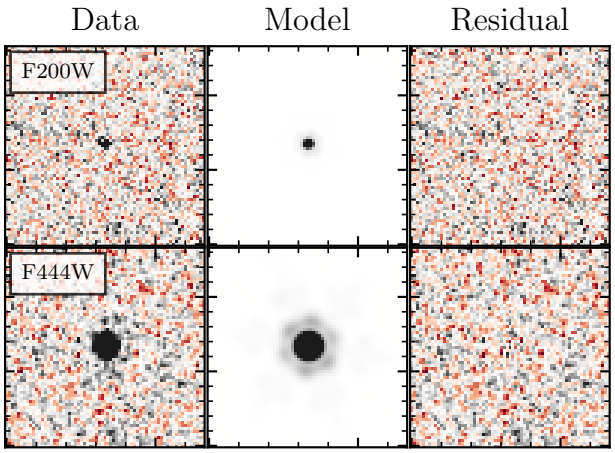

Figure 3. Results of 2D surface brightness profile fitting. We show $2'' \times 2''$ cutouts in F200W and F444W around CAPERS-LRD-z9 in the left column. Our best-fit point-source models in each band are shown in the middle column, while the residuals (data-model) are shown in the rightmost column. CAPERS-LRD-z9 is unresolved in all bands, with $r_h < 0\farcs04$ and $0\farcs08$ in F200W and F444W, respectively, corresponding to respective physical sizes of $\lesssim$175 pc and $\lesssim$350 pc.

$v_{\rm turb}$. These parameters predominantly impact the strength and shape of the Balmer break (see X. Ji et al. 2025) and are therefore important to model flexibly to optimize the fit. We adopt uniform priors for each parameter and again include a broadening of the AGN emission lines, a variable covering fraction of the BLR clouds (C_f), and dust attenuation (A_V; SMC law); we note that we explored allowing the attenuation curve slope to vary but find no need for an extremely steep dust law (in contrast to A. de Graaff et al. 2025).

For the galaxy model, we use the BPASS v2.2.1 stellar templates (E. R. Stanway & J. J. Eldridge 2018) and a flexible SFH via the "bursty continuity" parameterization described in S. Tacchella et al. (2023). We use five fixed age bins with edges at 0, 10, 30, 100, 200, and 300 Myr and a log-uniform prior on the stellar metallicity from 0.1% to 100% solar. We include nebular emission, varying log U from -4 to -1, and

Table 2
`Cloudy` Parameter Grid and Fitted Values

Parameter	Grid Values	Fitted Value
log $T_{\rm BB}$ (K)	4, 4.7, 5, 5.7	5.0
$\alpha_{\rm OX}$	-2.5, -2.0, -1.5	-1.5
$\alpha_{\rm UV}$	-0.1	...
$\alpha_{\rm X}$	-0.5	...
log $n_{\rm H}$ (cm^{-3})	9, 9.5, 10, 10.5, 11, 11.5, 12	$9.9^{+0.2}_{-0.2}$
$v_{\rm turb}$ (km s^{-1})	100, 200, 300, 400, 500	320^{+80}_{-60}
[Fe/H]	-2	...
log U	-3.5, -3, -2.5, -1.5, -0.5	-1.5
log $N_{\rm H}$ (cm^{-2})	21, 22, 23, 24, 25, 26	>25.9[a]
C_f	0–1	$0.12^{+0.01}_{-0.01}$
A_V	0–3 (SMC law)	$0.53^{+0.09}_{-0.08}$

Note. The first four parameters describe the incident continuum spectrum, where $T_{\rm BB}$ is the "big bump" temperature, $\alpha_{\rm OX}$ is the optical-to-X-ray index, $\alpha_{\rm UV}$ is the power-law UV slope, and $\alpha_{\rm X}$ is the power-law X-ray slope. The incident continuum is passed through dense gas defined by the gas density ($n_{\rm H}$), metallicity ([Fe/H]), and turbulent velocity ($v_{\rm turb}$). The level of irradiation at the face of the cloud is set by the ionization parameter (log U), and the `Cloudy` calculations are stopped at a range of line-of-sight column densities ($N_{\rm H}$).
[a] We provide the 1σ lower limit for the column density as our posterior is limited by the edge of the `Cloudy` grid.

dust attenuation (SMC law). Note that the dust attenuation is fit separately for the stars and AGN.

The final model is the combination of the stellar and AGN components, with the normalization of the latter fit as a free parameter. The model spectrum is convolved with the PRISM resolution curve, and the joint model is fit to both the NIRSpec spectrum and the NIRCam+MIRI photometry. We note that we mask the [O III] $\lambda\lambda$4959, 5007 doublet when fitting the spectrum, as the narrow-line region (NLR; see Section 4.4)—which is not considered in our `Cloudy` modeling of the BLR and nearby gas or our stellar model—may significantly contribute to these lines. We additionally mask the region

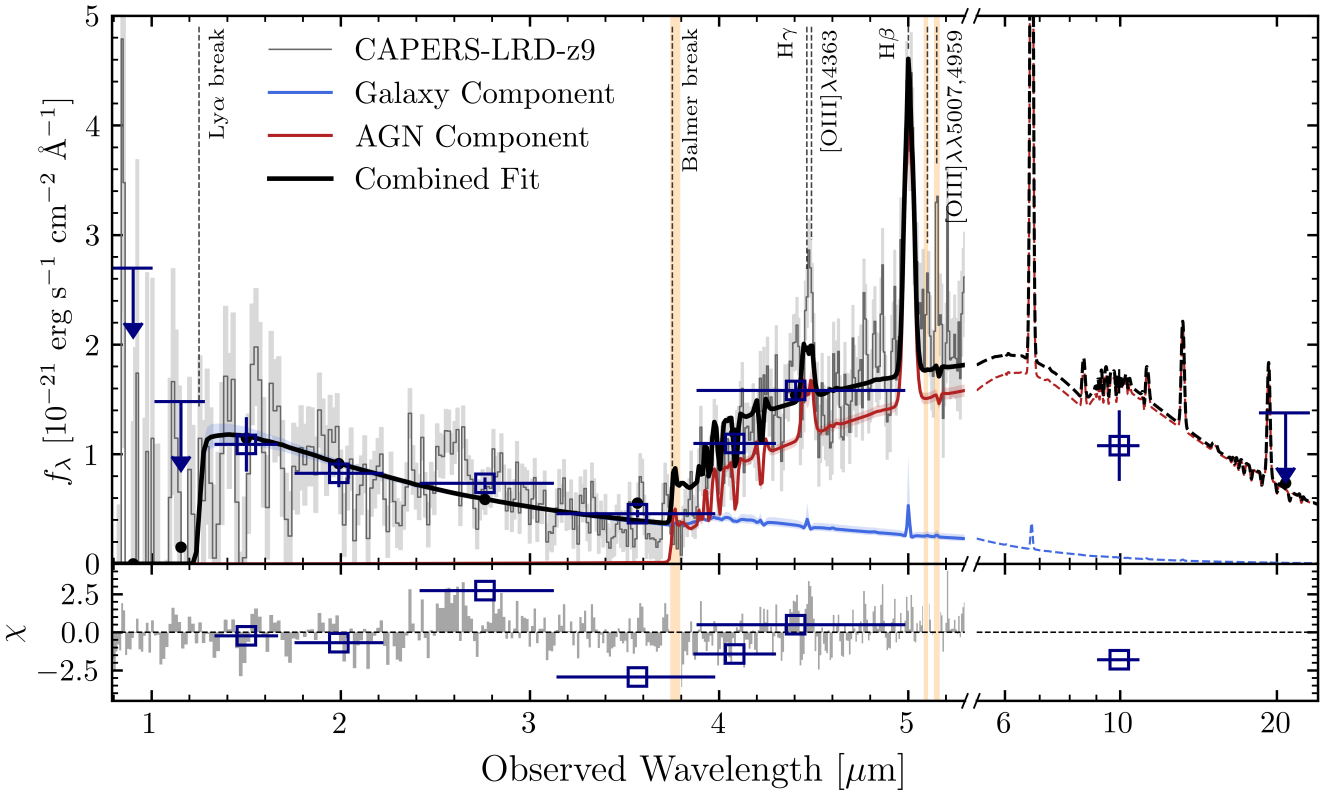

Figure 4. Spectrum and 1σ errors of CAPERS-LRD-z9 (gray curve, light gray shading), the best-fit host galaxy component (solid and dashed blue curves), the best-fit dense-gas-enshrouded AGN component (solid and dashed red curves), combined host+AGN fit (solid and dashed black curves), photometry data (dark blue squares and upper limits), best-fit model photometry (black points) in the upper panel, and masked regions (light orange shading). The lower panel shows the χ residuals of the fit for the spectrum (gray curve) and photometry (dark blue squares). Note that neither the `bagpipes` stellar model nor the `Cloudy` AGN model can match the strong [O III] λ4363 emission.

around H_∞ (3630–3690 Å), where the `Cloudy` modeling yields artifacts due to the finite number of resolved energy levels (K. Inayoshi & R. Maiolino 2025; X. Ji et al. 2025). The resulting best-fit model is shown in Figure 4, and the results from the spectrophotometric modeling are discussed in Sections 4.3 and 4.4.

4. Results

4.1. BLR Dust Attenuation

The ratio of observed fluxes from the Balmer series lines provides a measure of dust attenuation. Here we use the observed Hβ/Hγ ratio. As illustrated in Figure 2, the Hγ line is blended with [O III] λ4363. While we use priors based on the Hβ + [O III] $\lambda\lambda$4959, 5007 line widths to deblend these lines, the per-pixel S/N for Hγ is not sufficient for a double-component fit. Since we cannot isolate the narrow component of Hγ or Hβ, we compute a Balmer decrement for the BLR solely based on the ratio of the Hβ and Hγ broad components' fluxes, ensuring flux integration across comparable velocity ranges. This yields $H\beta/H\gamma = 3.5^{+1.7}_{-0.9}$.

To calculate A_V, we apply the SMC reddening law (K. D. Gordon et al. 2003), which has been found to match well the dust attenuation in high-z galaxies (P. L. Capak et al. 2015; N. A. Reddy et al. 2015, 2018) and reddened quasars (e.g., see A. M. Hopkins 2004). Assuming Case B recombination, the intrinsic line ratio would be $(H\beta/H\gamma)_{\rm int} = 2.14$ (D. E. Osterbrock 1989). Our observed ratio suggests significant attenuation; we estimate $A_{V,\rm BLR} = 1.9^{+1.3}_{-1.2}$ (where our precision is limited primarily by the S/N ≈ 4 detection of broad Hγ). We note that while Case B recombination may not be a sound assumption for collisionally excited gas, this nonetheless provides an estimate of the reddening of the BLR.

4.2. Black Hole Mass

Black hole mass estimation from broad emission lines relies on two fundamental assumptions: the broad-line emitting gas is virialized and dominated by the gravitational potential of the central black hole, and a "radius–luminosity" relationship exists between the broad-line orbital radius and the AGN luminosity (in Equation (1), the Hβ broad-line luminosity). These assumptions have generally been validated for low-redshift AGN (e.g., M. C. Bentz et al. 2006; E. M. Cackett et al. 2021), but their applicability to the broader AGN population is less certain.

In the specific case of CAPERS-LRD-z9, the broad and symmetric Hβ line profile is consistent with the basic virial assumption for kinematics dominated by gas orbits around a massive black hole, in contrast to the asymmetric broad-line profiles commonly observed in quasars with significant nonvirial kinematics (e.g., U. Vivian et al. 2022; L. B. Fries et al. 2024). The reliability of the radius–luminosity assumption is more difficult to assess. Compared to the radius–luminosity relation measured for Seyfert 1 AGN that was used to calibrate single-epoch masses, recent studies have shown that luminous and rapidly accreting quasars have smaller BLR

sizes (P. Du et al. 2016; G. Fonseca Alvarez et al. 2020), which leads to smaller black hole masses. The empirical radius–luminosity relation is generally assumed to be caused by a photoionization-bounded BLR (e.g., K. T. Korista & M. R. Goad 2004), and the unusual SED shape of LRDs like CAPERS-LRD-z9 could result in a significantly different BLR structure compared to other quasars. Elevated Eddington ratios also affect the radius–luminosity relation and may also result in the overestimation of black hole masses by as much as an order of magnitude (e.g.,. P. Du et al. 2016; A. Lupi et al. 2024). We ultimately use the canonical relationship for low-redshift AGN of Equation (1) to estimate a mass for CAPERS-LRD-z9 while acknowledging that significant work must be done to better understand the applicability of mass estimates for high-redshift LRDs.

To compute the canonical black hole mass, we use Equation (10) from J. E. Greene & L. C. Ho (2005), where $L_{H\beta}$ and $FWHM_{H\beta}$ are the luminosity and FWHM of the broad component of Hβ, respectively:

$$M_{BH} = (2.4 \pm 0.3) \times 10^6 \left(\frac{L_{H\beta}}{10^{42}\ \mathrm{erg\ s^{-1}}}\right)^{0.59\pm0.06} \times \left(\frac{FWHM_{H\beta}}{10^3\ \mathrm{km\ s^{-1}}}\right)^2 M_\odot. \quad (1)$$

Propagating the uncertainties on the calibration coefficients given in the empirical relation and the uncertainties on our line flux and FWHM, we derive a black hole mass for CAPERS-LRD-z9 of $\log(M_{BH}/M_\odot) = 7.58 \pm 0.15$. We note that additional systematic uncertainties from applying the J. E. Greene & L. C. Ho (2005) relations at high redshift may be as high as 0.5–0.7 dex (G. Fonseca Alvarez et al. 2020; R. Abuter et al. 2024).

To best capture these true systematic uncertainties and account for the limitations of our PRISM data, we next compute strong upper and lower limits on $\log(M_{BH}/M_\odot)$. First, we derive an upper bound by correcting our canonical measurement for dust attenuation. By adopting the estimated reddening of $A_{V,BLR} = 1.9^{+1.3}_{-1.2}$ (computed above), we derive a higher black hole mass of $\log(M_{BH}/M_\odot) = 8.10 \pm 0.40$. Using our $A_V \approx 0.53$ from our spectrophotometric fitting, we alternatively compute $\log(M_{BH}/M_\odot) = 7.70 \pm 0.14$. We note that while our Balmer-decrement-based and spectrophotometric-fitting-based A_V values are discrepant at the 1.3σ level, we attribute this difference to the uncertain assumption of Case B recombination in the BLR, uncertainty on the Hγ line flux due to the limitations of the PRISM resolution, and possible collisional deexcitation of neutral gas in the dense gas region of the LRD. Nonetheless, we adopt the 1σ upper limit on the Balmer-decrement-derived value ($\log(M_{BH}/M_\odot) < 8.5$) as a strong upper limit on the black hole mass.

We also compute a lower limit on the black hole mass using the Hβ line luminosity and assuming that the AGN is accreting at the Eddington rate. For the purposes of computing a lower limit, we conservatively convert the Hβ luminosity to Hα luminosity assuming an unattenuated Case B ratio (Hα/Hβ = 2.86; D. E. Osterbrock 1989) and use the bolometric correction from J. Stern & A. Laor (2012) to derive $\log(M_{BH}/M_\odot) > 6.65$. This method has the benefit of being insensitive to the measured Hβ line width. As such, it remains robust even if the Hβ line width is significantly overestimated due to uncertainties in the effects of the NIRSpec/PRISM spectral resolution or more exotic explanations for line broadening, such as electron scattering (e.g., V. Rusakov et al. 2025).

When considering these upper and lower limits together, we compute systematic bounds on $\log(M_{BH}/M_\odot)$ of 6.65–8.50. However, for ease of comparisons to other reported LRD black hole masses in the literature, we adopt our canonical measurement and its associated nonsystemic error bounds for the remainder of this work (unless otherwise stated).

4.3. Stellar Mass

Properly estimating the stellar masses of LRDs has proven enormously difficult given the unclear origin of the "V-shaped" spectrum and degeneracies in decomposing the galaxy/AGN contribution (e.g., G. Barro et al. 2024a; V. Kokorev et al. 2023; L. H. B. Akins et al. 2024; L. J. Furtak et al. 2024; I. Labbe et al. 2024; B. Wang et al. 2025, 2024b). Here, we have assumed that the rest-UV is dominated by stars (with the rest-optical dominated by the AGN); however, we do not know this a priori. The stellar mass we derive is likely therefore an upper limit, as it is entirely possible that the UV is also AGN-dominated (a possibility we discuss further in Section 5.3). The joint `bagpipes+Cloudy` fitting described in Section 3.4 yields a host galaxy stellar mass of $\log(M_*/M_\odot) = 8.9^{+0.1}_{-0.1}$.

We note that stellar masses can be underestimated when derived from the UV alone due to "outshining" from young O/B stars (see, e.g., D. Narayanan et al. 2024). However, as there are no prominent emission features in the rest-UV of CAPERS-LRD-z9, and the rest-optical emission lines are accounted for via the AGN, the SFH model is not biased toward a young stellar population. In fact, the age–dust–metallicity degeneracy is accounted for in our posterior estimate. We explored including an additional burst of SF at $z = 20$, and found a consistent stellar mass with no meaningful improvement to the quality of the fit, showing that the observations do not allow for a significant mass in older stars to be present in this object.

From our computed stellar mass upper limit and our canonical measurement of M_{BH}, we compute $M_{BH}/M_* > 4.5\%$. Invoking our systematic lower and upper bounds for M_{BH}, we alternatively compute $M_{BH}/M_* > 0.5\%$ and $M_{BH}/M_* > 46\%$, respectively. We plot this black hole to stellar mass ratio in Figure 5, along with a large body of literature samples (Y. Harikane et al. 2023; D. D. Kocevski et al. 2023, 2025; V. Kokorev et al. 2023, 2024a; R. L. Larson et al. 2023; L. J. Furtak et al. 2024; I. Labbe et al. 2024; R. Maiolino et al. 2024; R. Tripodi et al. 2024; H. Übler et al. 2024; B. Wang et al. 2025; M. Yue et al. 2024b; H. B. Akins et al. 2025a; I. Juodžbalis et al. 2025). Figure 5 demonstrates the "overmassiveness" of CAPERS-LRD-z9 in the context of both literature samples of JWST-detected AGN (colored points) as well as the established mass ratio for local quasars of 0.1% (dashed black line). For comparison, we overlay the predicted evolution of M_{BH}/M_* ratios from $\sim 10^3$ early black hole populations formed via two distinct seeding channels: heavy seeds (red contours) and light seeds (blue contours), based on the SP1 model presented in H. Hu et al. (2025).

The observed value of CAPERS-LRD-z9 is broadly consistent with both scenarios, but the lower limit nature of

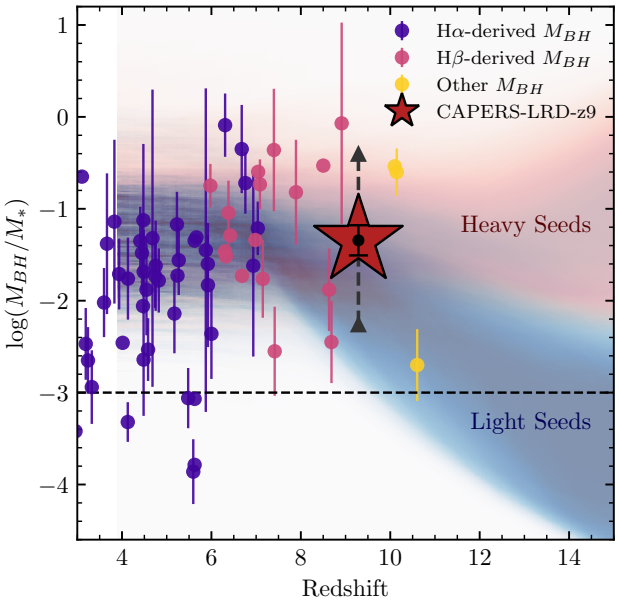

Figure 5. Black hole mass to stellar mass ratio $\log(M_{\rm BH}/M_*)$ as a function of redshift for CAPERS-LRD-z9 (red star) and a collection of literature JWST-detected AGN (Y. Harikane et al. 2023; D. D. Kocevski et al. 2023, 2025; V. Kokorev et al. 2023, 2024a; R. L. Larson et al. 2023; Á. Bogdán et al. 2024; L. J. Furtak et al. 2024; I. Labbe et al. 2024; R. Maiolino et al. 2024; L. Napolitano et al. 2024; R. Tripodi et al. 2024; H. Übler et al. 2024; B. Wang et al. 2025; M. Yue et al. 2024b; H. B. Akins et al. 2025a; I. Juodžbalis et al. 2025), showing the published errors, typically exclusive of systematic uncertainties. We divide the literature-selected samples into those selected based on a broad Hα line (purple points), a broad Hβ line (pink points), and based on UV line or X-ray detections (yellow points). We plot the statistical errors on CAPERS-LRD-z9 as the black error bars, and we include a larger systematic range on $\log(M_{\rm BH}/M_*)$ based on the systematic limits on the black hole mass of CAPERS-LRD-z9 as a gray dashed line and upward-pointing arrows. We stress that as our M_* measurement is an upper limit, all of our measurements of $M_{\rm BH}/M_*$ are lower limits. We plot the $M_{\rm BH}/M_* = 0.1\%$ value for local galaxies as a black dashed line. For comparison, we overlay the predicted evolution of $M_{\rm BH}/M_*$ ratios from early black hole populations formed via two distinct seeding channels: heavy seeds (red shaded region) and light seeds (blue shaded region), based on the semianalytical model presented in H. Hu et al. (2025). The population of JWST-detected AGN exhibits an apparent overmassiveness in this ratio compared to the local relation.

this value may hint toward the heavy-seed regime. We discuss possible explanations for this effect and its possible interplay with black hole seeding and growth in Section 5.1.

4.4. Gas Density and Temperature

Our best-fit AGN model has $\log n_{\rm H}/{\rm cm}^{-3} \sim 9.9^{+0.2}_{-0.2}$ and $\log N_{\rm H}/{\rm cm}^{-2} \gtrsim 26$.[40] These are similar to the best-fitting parameters for MoM-BH*-1 and RUBIES-UDS-154183 (A. de Graaff et al. 2025; R. P. Naidu et al. 2025) and suggest very extreme gas conditions in the BLR. To examine whether these conditions extend to the NLR, we look to the forbidden oxygen lines. We measure an extremely high ratio of [O III] λ4363/[O III] λ5007 (RO3) = 0.58 $\pm$ 0.23 in CAPERS-LRD-z9. Though [O III] λ4363 is blended with Hγ at the PRISM resolution, our MCMC line fitting (described in Section 3.2) yields a significant [O III] detection (S/N $\sim$ 3).

As the [O III] λ4363 and λ5007 lines arise from different upper energy levels, RO3 is commonly used as a temperature diagnostic. High RO3 traces high-temperature regions of the ISM and is found to be increasingly common in $z \gtrsim 8$ galaxies (J. Brinchmann 2023; H. Katz et al. 2023; F. Cullen et al. 2025). RO3 has also been used as an AGN diagnostic, particularly at high redshift, where the canonical Baldwin, Phillips, and Terlevich diagram breaks down due to lower metallicity (B. E. Backhaus et al. 2023; G. Mazzolari et al. 2024). Here, the [O III] λ4363 line likely traces the NLR or ISM gas heated by the AGN in addition to star formation.

The ratio we observe for CAPERS-LRD-z9 (RO3 $\approx$ 0.58 $\pm$ 0.23) is particularly extreme, even compared to other $z > 7$ BLAGN (V. Kokorev et al. 2023; R. Tripodi et al. 2024; H. Übler et al. 2024). Such a high ratio is only possible at densities approaching (or exceeding) the critical density of [O III] λ5007 ($n_e \sim 7 \times 10^5\,{\rm cm}^{-3}$), where collisional deexcitation becomes important. The critical density for [O III] λ4363 is significantly higher ($\sim 10^8\,{\rm cm}^{-3}$). Using `pyneb` (V. Luridiana et al. 2015), we find that the RO3 we measure corresponds to densities $\gtrsim 10^6\,{\rm cm}^{-3}$, even at very high temperatures of $T_e \sim 10^5$ K. At lower temperatures ($T_e \sim 10^4$ K), the implied density is even higher: $n_e \gtrsim 10^8\,{\rm cm}^{-3}$. This suggests that the NLR itself could be quite dense, corroborating the extreme densities inferred for the BLR.

5. Discussion

5.1. Implications for Black Hole Seeding and Growth

We plot our canonical black hole mass for CAPERS-LRD-z9 in Figure 6, along with other notable $z > 6$ AGN from the literature. We also plot simple models of Eddington-limited black hole growth (with 10% radiative efficiency) for both stellar (light) seeds ($\sim 10^2\,M_\odot$) and more massive heavy seeds ($\gtrsim 10^4\,M_\odot$). The red shaded region corresponds to heavy seeds with formation redshifts of 25–15 that begin accreting at the Eddington limit immediately after formation. For the stellar remnant light seeds, we plot formation redshifts of 30–15 and require an additional 100 Myr to pass after the formation redshift before accretion begins due to progenitor gas heating by the precollapsed stars (e.g., J. L. Johnson & V. Bromm 2007). It is clear that CAPERS-LRD-z9's SMBH is too massive to form from a simple stellar remnant that grows at the Eddington rate, similar to what has been inferred for other recently discovered high-z AGN (e.g., R. L. Larson et al. 2023). However, a heavy seed growing at the Eddington rate can easily reproduce the observed black hole mass, making it a plausible formation pathway. This scenario naturally establishes the overmassive $M_{\rm BH}/M_*$ configurations present at high z, as shown in Figure 5 (see also the red shading representing the heavy-seed model prediction). Furthermore, the emerging SMBH demographics suggest that the black hole to stellar mass ratio may bifurcate into high- and low-$M_{\rm BH}/M_*$ branches as we approach the highest redshifts. Such a bifurcation has been predicted for a hybrid seeding scenario, where the two branches are linked to heavy and light seeds, respectively (also see Figure 3 in J. Jeon et al. 2025b).

A key uncertainty in all direct-collapse black hole (DCBH) models is the choice of formation criteria, such as the required level of soft-UV (Lyman–Werner) background flux or the critical metallicity above which gas cooling would become too efficient, resulting in cloud fragmentation that suppresses DCBH formation (e.g., V. Bromm & A. Loeb 2003; M. C. Begelman et al. 2006; K. Omukai et al. 2008; J. H. Wise et al. 2019). The value of these parameters is reflected in the

[40] Note that these results describe a Compton-thick regime that `Cloudy` is not explicitly designed to model (see Section 3.4).

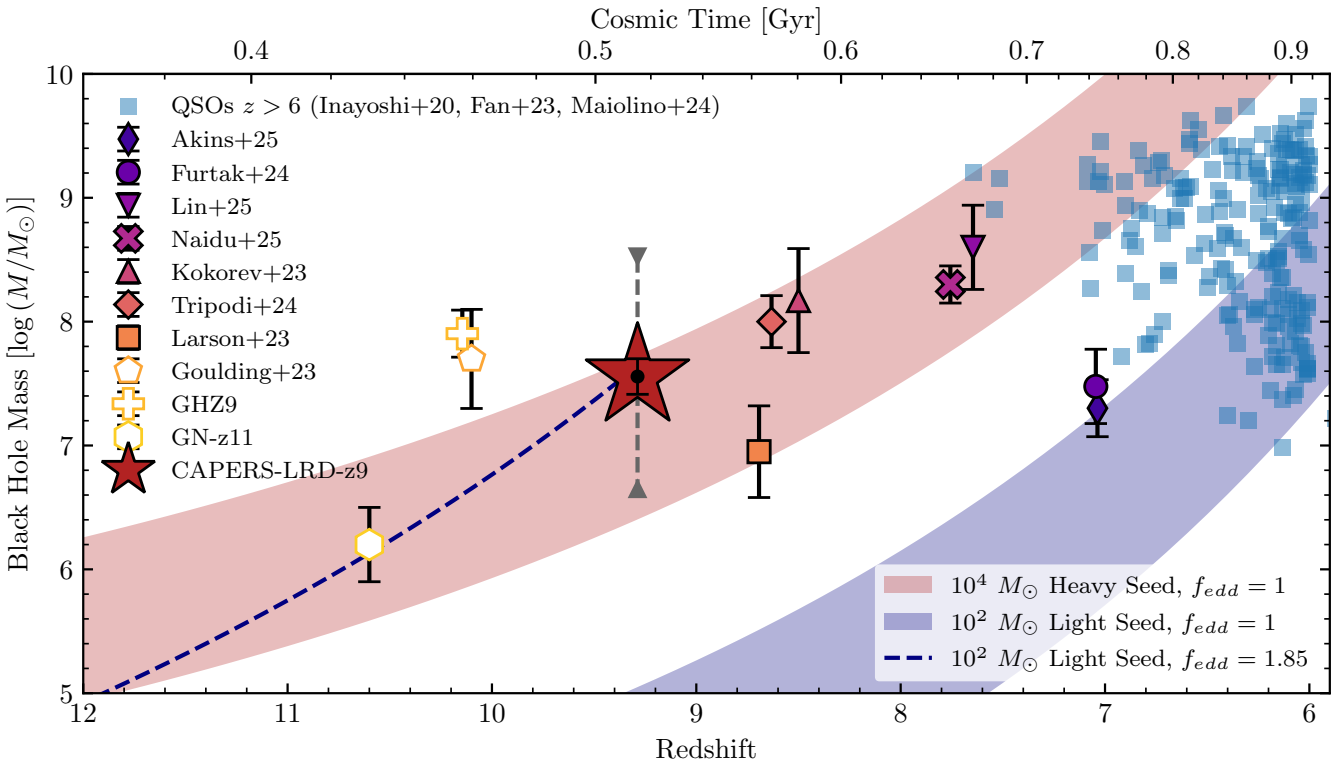

Figure 6. Redshifts and black hole masses of CAPERS-LRD-z9 (red star; canonical errors are shown in black, systematic upper and lower limits are shown in gray), populations of $z \gtrsim 6$ quasars (small blue points; K. Inayoshi et al. 2020; X. Fan et al. 2023; R. Maiolino et al. 2024), notable massive $z > 6$ spectroscopically confirmed BLAGN (filled symbols; V. Kokorev et al. 2023; R. L. Larson et al. 2023; L. J. Furtak et al. 2024; R. Tripodi et al. 2024; H. B. Akins et al. 2025a; X. Lin et al. 2025; R. P. Naidu et al. 2025), and the highest-redshift AGN detected through X-ray emission and high-ionization UV emission lines, respectively (open symbols; A. J. Bunker et al. 2023; A. D. Goulding et al. 2023; O. E. Kovács et al. 2024; L. Napolitano et al. 2024). We also show the growth of $10^2\ M_\odot$ (blue shading) and $10^4\ M_\odot$ (red shading) black hole seeds growing at the Eddington limit. We also show the growth track of a $10^2\ M_\odot$ stellar remnant formed at $z = 30$ that starts accreting at 1.85× the Eddington limit 100 Myr after formation (dark blue dashed curve). CAPERS-LRD-z9's black hole is too massive to be the result of an Eddington-limited stellar seed; thus, a stellar remnant light seed undergoing periods of super-Eddington accretion or a heavy seed are necessary to produce CAPERS-LRD-z9's black hole by $z = 9.288$.

resulting number densities of DCBH seeds and their descendants (e.g., A. Trinca et al. 2022; H. Hu et al. 2025; J. Jeon et al. 2025b). In turn, any firm limits on the DCBH abundance would significantly constrain the formation scenarios, as could be accomplished by linking the DCBH seeding pathway to a subset of the observed LRD population.

Some studies have suggested that the conditions required to form DCBH seeds are too rare for this channel to account for the majority of the SMBHs being detected by JWST (e.g., A. K. Bhowmick et al. 2024), whereas others argue for less restrictive conditions (e.g., S. Chon & K. Omukai 2025). However, observations suggest that ultradense star clusters may be common or even ubiquitous in high-redshift galaxies (A. Adamo et al. 2024; S. Fujimoto et al. 2024; L. Mowla et al. 2024), providing a promising additional heavy-seeding mechanism.

Furthermore, the heavy-seed explanation is not the only way to produce CAPERS-LRD-z9's black hole mass by $z = 9.288$. Allowing (even mild) super-Eddington accretion with a stellar remnant seed can also reproduce the black hole mass of CAPERS-LRD-z9. For example, in Figure 6, we show that a $10^2\ M_\odot$ stellar remnant formed at $z = 30$ growing at an average Eddington ratio of 1.85 after a 100 Myr delay in starting accretion can easily reproduce the black hole mass of CAPERS-LRD-z9. In reality, we expect that super-Eddington accretion occurs in short bursts (e.g., E. Takeo et al. 2020; H. Suh et al. 2025). However, we plot the simplified average Eddington ratio growth curve here for visual clarity.

5.2. A Dense Gas Origin?

As referenced in Section 1, the "dense gas" model of LRDs has garnered significant attention in the literature in recent months. This model, introduced by K. Inayoshi & R. Maiolino (2025), has recently been applied to two newly discovered LRDs—MoM-BH*-1 at $z = 7.76$ (R. P. Naidu et al. 2025) and RUBIES-UDS-154183 at $z = 3.55$ (A. de Graaff et al. 2025)—as well as the triply imaged $z = 7.04$ LRD A2744-QSO1 (L. J. Furtak et al. 2024; X. Ji et al. 2025). We plot these objects, and the $z = 4.47$ LRD (UNCOVER-45924) from I. Labbe et al. (2024), in Figure 7. All spectra are normalized to the spectrum of CAPERS-LRD-z9 at rest-frame 0.51 μm.

All of these objects are notable for their strong Balmer breaks, which, in the cases of MoM-BH*-1 and RUBIES-UDS-154183, were insufficiently fit by evolved stellar populations (A. de Graaff et al. 2025; R. P. Naidu et al. 2025). The Balmer breaks and SEDs of both objects were better fit by invoking the dense gas model of K. Inayoshi & R. Maiolino (2025). Similarly, while another object—A2744-45924—can be fit with a stellar model, the implied stellar mass is large ($\sim 10^{11}\ M_\odot$) and in tension with the Atacama Large Millimeter/submillimeter Array dynamical mass measurement of $\sim 10^9\ M_\odot$ (H. B. Akins et al. 2025b).

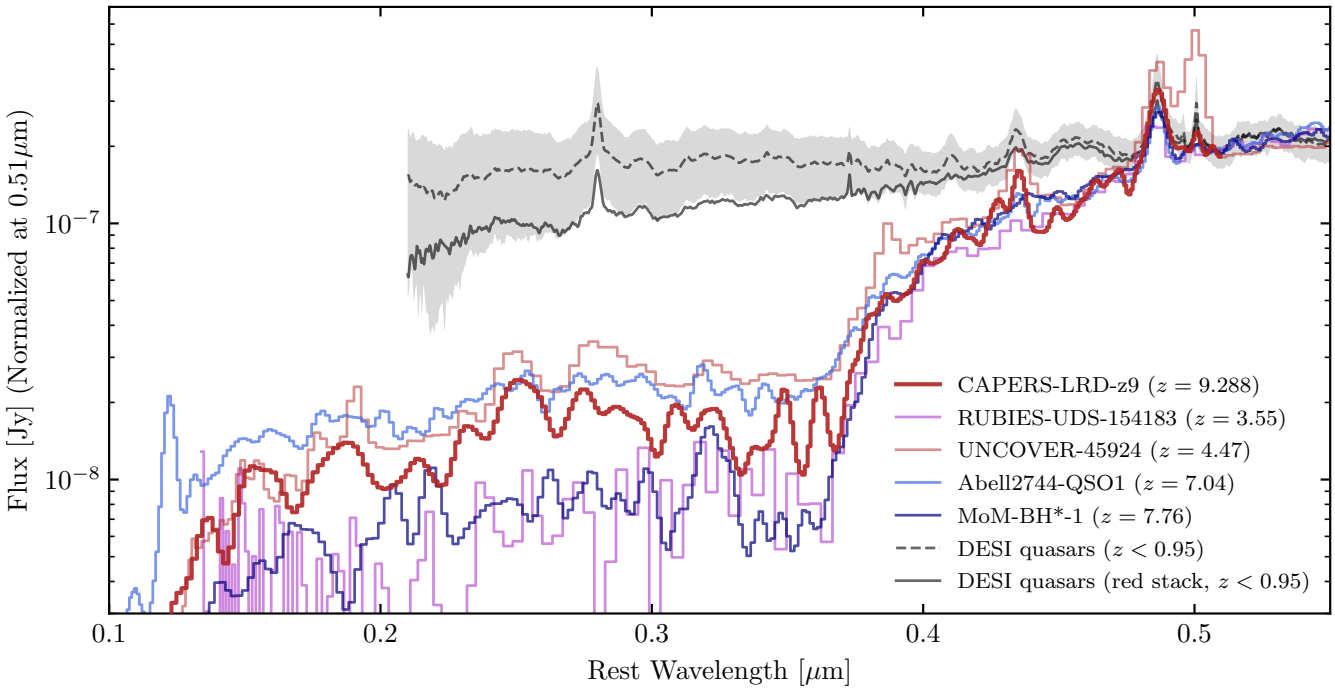

Figure 7. The NIRSpec MSA/PRISM spectra of CAPERS-LRD-z9, MoM-BH*-1 at $z = 7.76$ (R. P. Naidu et al. 2025), RUBIES-UDS-154183 at $z = 3.55$ (A. de Graaff et al. 2025), UNCOVER-45924 at $z = 4.47$ (I. Labbe et al. 2024), and A2744-QSO1 at $z = 7.04$ (L. J. Furtak et al. 2024; X. Ji et al. 2025) normalized to the spectrum of CAPERS-LRD-z9 at rest-frame 0.51 μm. We apply a 1–2 pixel Gaussian smoothing (smoothing lower-z objects less, as they are already relatively smoothed by PRISM's lower spectral resolution at bluer observed wavelengths) to all five spectra to increase visual clarity. For comparison, we plot the median and 10th–90th percentile of DESI spectra of 232 quasars ($z < 0.95$) selected to have similar values of H$\beta_{\rm broad}$ FWHM, L([O III] λ5007), and [O III] λ5007/Hβ flux ratio (gray shading and gray dashed curve) and the stack of the reddest 20 DESI quasars (gray solid curve). While the rest-optical emission from CAPERS-LRD-z9 strongly resembles that of the other NIRSpec sources, these sources are all starkly different from quasars identified in DESI, where even the reddest DESI quasars fail to approach the reddening or Balmer break exhibited in the NIRSpec LRDs.

While CAPERS-LRD-z9 shows a factor of $\sim$1.5 softer break ($f_{\nu,4050\,\text{Å}}/f_{\nu,3670\,\text{Å}} = 4.35^{+0.93}_{-0.67}$) than MoM-BH*-1 ($7.7^{+2.3}_{-1.4}$) and RUBIES-UDS-154183 ($6.9^{+2.8}_{-1.5}$), all of these objects show a remarkably similar rest-frame optical SED and Balmer break shape, suggesting common physical and emission structures. However, unlike MoM-BH*-1, CAPERS-LRD-z9 demonstrates only moderate Hβ absorption and shows a strong detection of Hγ in emission. Higher-resolution spectroscopy of CAPERS-LRD-z9 beyond that of NIRSpec/PRISM would allow for a higher-fidelity examination of these features.

Given the similarity in spectral shapes between CAPERS-LRD-z9 and the sources in A. de Graaff et al. (2025) and R. P. Naidu et al. (2025), we propose that the rest-frame optical light from CAPERS-LRD-z9 is indeed dominated by AGN emission through a shell of dense ($\gtrsim 10^{10}$ cm^{-3}) neutral gas, and that the rest-UV emission blueward of the Balmer break may be stellar emission from the host galaxy (e.g., D. D. Kocevski et al. 2023) or scattered light originating from the AGN (e.g., J. E. Greene et al. 2024). From our `Cloudy` modeling, we infer a gas density of $\log n_{\rm H}/{\rm cm}^{-3} = 9.9^{+0.2}_{-0.2}$ and column density $\log N_{\rm H}/{\rm cm}^{-2} \gtrsim 26$. These results are remarkably comparable to MoM-BH*-1 and RUBIES-UDS-154183, further suggesting that these objects may have similarities in their physical structure. However, we note that this dense regime is beyond `Cloudy`'s recommended use cases, and alternate analyses may be necessary in future work to fully understand the nature of these exotic sources.

We also note that our best-fit spectrophotometric model overpredicts the MIRI F1000W flux by $\chi = -1.8$. These data were used in the fitting procedure, but the model was not flexible enough to simultaneously fit the NIRSpec+MIRI data. We attempt to better match the MIRI photometry by including a flexible dust attenuation law for the AGN component of the model (see the Appendix for details). In this revised fit, we find a best-fit S. Salim et al. (2018) δ parameter—which governs the steepness of the attenuation curve, with negative values producing increasingly steeper curves—of $\delta = -4.66^{+0.31}_{-0.24}$. While the resulting fit matches the MIRI F1000W flux with $\chi = -0.27$ with no detrimental effects on the rest of the fit, $\delta = -4.66$ represents an attenuation curve that is unphysically steep, as it is by definition a D. Calzetti (2001) curve multiplied by an additional factor of $(\lambda/5500\,\text{Å})^{4.66}$. For reference, an SMC law can be approximated with a comparatively small $\delta = -0.45$. While steep attenuation curves were also explored in A. de Graaff et al. (2025) to reconcile their MIRI observations with the dense gas LRD model, we agree with their assessment that such curves are likely unrealistic. Alternate models and modeling parameters are thus necessary to reproduce the rest-NIR properties of the LRDs, including—perhaps—modifying the intrinsic SED of the accretion disk. Such modeling may soon be robustly enabled by the increasing known population of dense gas modeled LRDs.

In terms of the overall assembly history of the first SMBHs, we may witness a three-stage evolutionary sequence: the initial seeding process, a period of rapid growth during the LRD stage driven by massive inflows of gas, and a final "clearing of the fog" (possibly driven by radiation-hydrodynamics processes; e.g., A. Smith et al. 2017), when the emerging SMBHs become unobscured and, with sufficient cosmic time to assemble additional stellar mass, join the "standard" quasar/AGN sequences at lower redshifts. More specifically, K. Inayoshi (2025) proposed that LRDs may be simply the first incidence of

AGN activity in a galaxy's evolution, based on the log-normal occurrence rate of LRDs with cosmic time. The nascent evolutionary stage of the LRDs in this toy model may also explain their unique and extreme characteristics. The SMBH could form early in a galaxy's lifespan, surrounded by a large reservoir of dense neutral gas that serves as both a readily available supply of accretion material and the shell of dense gas surrounding the AGN (as in K. Inayoshi & R. Maiolino 2025). This scenario would result in an overmassive SMBH producing a dense gas reddened SED with a strong Balmer break, in combination with nascent star formation in the host galaxy that produces a blue rest-UV slope. In summation, these two components would supply the two halves of the defining LRD "V-shaped" SED for the duration of the initial "LRD phase" of AGN activity. Given the low metallicity/dust content but high column density of the nuclear gas, this model also favorably reproduces the lack of mid-IR dust emission (H. B. Akins et al. 2024; G. C. K. Leung et al. 2024; P. G. Pérez-González et al. 2024; C. C. Williams et al. 2024) and lack of X-rays (E. Lambrides et al. 2024; M. Yue et al. 2024a; R. Maiolino et al. 2025) observed in LRDs. During future AGN active periods—after a period of dormancy—the stellar mass of the galaxy will have had sufficient time to accumulate and produce a more typical black hole to stellar mass ratio of $M_{\rm BH}/M_* = 0.1\%$. Simultaneously, the dense gas near the AGN will be consumed by the AGN during the LRD phase, such that in future instances of AGN activity, the resulting evolved galaxy and AGN resemble a classical quasar/AGN.

5.3. A Nonstellar Origin for the UV Continuum?

In Section 4.3, we have estimated the stellar mass of the host galaxy of CAPERS-LRD-z9 under the assumption that its UV luminosity is primarily powered by star formation. Even a visual inspection, however, shows that the shape of the UV continuum is unlike that of star-forming galaxies at comparable redshifts (e.g., M. Castellano et al. 2022; V. Kokorev et al. 2025). As Figure 7 illustrates, despite the relatively low S/N, the slope of the continuum of CAPERS-LRD-z9 appears to change at around rest-frame ≈2500 Å, redward of which is relatively blue and rising toward shorter wavelengths, whereas at bluer wavelengths, it flattens and then perhaps decreases. Moreover, at rest-frame ≈2500 Å (observed-frame 2.6 μm), there is a hint of an apparent broad emission feature (see Figures 1 and 4). Figure 7 also shows an overall similarity between the UV continuum of CAPERS-LRD-z9 and that of UNCOVER-45924, which has a substantially higher S/N, and strong UV lines such as C IV λ1550 and C III] λ1908 and the Fe II lines commonly seen in quasars (e.g., M. Vestergaard & B. J. Wilkes 2001). These features are not detected with statistical significance in the spectrum of CAPERS-LRD-z9, yet the broad emission feature at ≈2500 Å may be associated with the Fe II pseudocontinuum, as in A2744-45924. This, as well as the overall shape of the continuum, is intriguing and adds credence to the idea that the UV continuum in CAPERS-LRD-z9 could be nonstellar.

To further explore this idea, we compare the LRDs to a control sample of quasars ($z < 0.95$) from the Dark Energy Spectroscopic Instrument (DESI) DR1 data set (DESI Collaboration et al. 2025). We assemble this sample by selecting DESI quasars with similar H$\beta_{\rm broad}$ FWHM, L([O III] λ5007), and [O III] λ5007/H$\beta_{\rm total}$ flux ratios to CAPERS-LRD-z9 based on `FastSpecFit` (J. Moustakas et al. 2023) emission line measurements reported in the DESI AGN/QSO value-added catalog[41] (S. Juneau et al. 2025, in preparation). We plot both the 10th–90th percentile of these objects and the inverse-variance-weighted mean stack of the 20 reddest objects in Figure 7 as a standard of comparison. It is immediately clear that even the stack of the reddest DESI quasars strongly differs from the LRD rest-optical continua, including a lack of the prominent Fe II bump at 4434–4684 Å in the LRDs (which is not expected to appear in faint [$L_{\rm H\beta} < 10^{44}$ erg s^{-1}] high-redshift AGN; e.g., B. Trefoloni et al. 2024). However, as mentioned above, in the rest-UV, CAPERS-LRD-z9 and UNCOVER-45924 both exhibit possible AGN signature emission features such as the ∼0.25 μm iron bump, prominently featured in the DESI stack, suggesting that the rest-UV emission may indeed have an AGN origin.

The question naturally arises how UV emission from the accretion disk can escape such a dense gas cloud. As suggested by J. E. Greene et al. (2024), the rest-UV light in LRDs could originate from accretion disk photons being either scattered or directly transmitted (via a patchy medium). If we simply rescale the rest-UV continuum from the DESI quasars shown in Figure 7 to match our data, we find that the UV slopes are roughly consistent with an implied scattering fraction of ∼10%, fully consistent with the results presented in J. E. Greene et al. (2024). The scattering medium could be neutral (Rayleigh scattering) or partially ionized gas (Rayleigh and Thomson scattering) and could be associated with either the external regions of the same dense gaseous envelope that enshrouds the AGN or different regions altogether. The type of scattering medium and its geometry will, in general, contribute to the overall spectral shape and intensity, given the specific wavelength dependence of the scattered radiation, and this might also help explain the diversity of spectral morphologies observed in this category of sources.

If the UV emission is predominantly of AGN origin, the upper limit to the stellar mass discussed in Section 4.3 will have to be revised downward by a substantial amount, which is unconstrained by the current data. This makes the ratio $M_{\rm BH}/M_* \gg 4.5\%$ substantially more extreme, with important implications for the mechanisms of formation and coevolution of SMBHs and their host galaxies.

6. Summary

In this work, we spectroscopically confirm and analyze the highest-redshift BLAGN observed to date: CAPERS-LRD-z9. We summarize our primary results below.

1. Using JWST/NIRSpec PRISM spectroscopy from the CAPERS program, we identify the highest-redshift ($z = 9.288$) BLAGN yet discovered—CAPERS-LRD-z9—based on a strong detection of broad (FWHM = 3525 ± 589 km s^{-1}) Hβ emission.
2. We determine that CAPERS-LRD-z9 is unresolved in NIRCam imaging, placing upper limits of $\lesssim$175 pc and $\lesssim$350 pc on its physical size in the rest-UV and rest-optical.
3. We use the J. E. Greene & L. C. Ho (2005) empirical relations to estimate a black hole mass of $\log(M_{\rm BH}/M_\odot) = 7.58 \pm 0.15$. We place conservative bounds on this mass measurement, accounting for systematic uncertainties, by assuming Eddington-limited

[41] https://data.desi.lbl.gov/doc/releases/dr1/vac/agnqso/

accretion (lower bound) and applying a dust correction based on the Balmer decrement (upper bound). This yields a range of $\log(M_{\rm BH}/M_\odot) = 6.65$–$8.50$.

4. We successfully model CAPERS-LRD-z9 as an AGN enshrouded in a shell of dense ($n_{\rm H} > 10^9$ cm^{-3}) neutral gas using `Cloudy` following the models of K. Inayoshi & R. Maiolino (2025) that have been recently applied to similar sources (A. de Graaff et al. 2025; X. Ji et al. 2025; R. P. Naidu et al. 2025). We fit the rest-frame UV to a stellar population model using `bagpipes`. From this modeling, we derive an upper limit on the host galaxy stellar mass of $<10^9\ M_\odot$ and estimate a neutral gas density near the AGN of $n_{\rm H} \sim 10^{10}$ cm^{-3}.
5. From our canonical black hole mass, we calculate a black hole mass to stellar mass ratio $M_{\rm BH}/M_* > 4.5\%$ for CAPERS-LRD-z9. However, we recognize that our estimates of both $M_{\rm BH}$ and M_* are subject to large systematic uncertainties. Based on our systematic bounds of $M_{\rm BH}$, the lower limit on $M_{\rm BH}/M_*$ ranges from $>46\%$ to as low as $>0.5\%$. Even our absolute lowest bound presents a significant deviation from the "typical" $M_{\rm BH}/M_* \sim 0.1\%$ value exhibited by local quasars.
6. We model the growth of the SMBH powering CAPERS-LRD-z9 and find that an Eddington-limited heavy ($\sim 10^4\ M_\odot$) seed or a super-Eddington light ($\sim 10^2\ M_\odot$) seed are necessary to produce such an SMBH by $z = 9.288$.

From these results, it is clear that CAPERS-LRD-z9 is an extreme example of an LRD in redshift, $M_{\rm BH}/M_*$, and neutral gas density. Along with MoM-BH*-1 and RUBIES-UDS-154183, CAPERS-LRD-z9 provides strong evidence in support of the "dense-gas-enshrouded AGN" physical explanation for the rest-frame optical emission from LRDs. Furthermore, its unprecedented redshift for a BLAGN provides insight into the interplay between black hole formation and growth and the physical properties of LRDs. While we present an initial analysis of CAPERS-LRD-z9 in this work, further analysis of such an exotic source will undoubtedly continue to enhance our understanding of galaxy, AGN, and SMBH evolution in the very early Universe.

Acknowledgments

A.J.T. acknowledges support from the UT Austin College of Natural Sciences, and A.J.T. and S.L.F. acknowledge support from STScI/NASA through JWST-GO-6368. A.C.C. and H.L. acknowledge support from a UKRI Frontier Research Guarantee Grant (PI: Carnall; grant reference EP/Y037065/1). L.N. acknowledges support from grant "Progetti per Avvio alla Ricerca—Tipo 1, Unveiling Cosmic Dawn: Galaxy Evolution with CAPERS" (AR1241906F947685). J.S.D. acknowledges the support of the Royal Society via the award of a Royal Society Research Professorship. R.A. acknowledges the support of grant PID2023-147386NB-I00 funded by MICIU/AEI/10.13039/501100011033 and by ERDF/EU and the Severo Ochoa grant CEX2021-001131-S funded by MCIN/AEI/10.13039/50110001103. F.C. and T.M.S. acknowledge support from a UKRI Frontier Research Guarantee Grant (PI: Cullen; grant reference EP/X021025/1). K.I. acknowledges support from the National Natural Science Foundation of China (12233001), the National Key R&D Program of China (2022YFF0503401), and the China Manned Space Program (CMS-CSST-2025-A09).

This work is based on observations made with the NASA/ESA/CSA James Webb Space Telescope, obtained at the Space Telescope Science Institute, which is operated by the Association of Universities for Research in Astronomy, Incorporated, under NASA contract NAS5-03127. Support for program number GO-6368 was provided through a grant from the STScI under NASA contract NAS5-03127. The data were obtained from the Mikulski Archive for Space Telescopes (MAST) at the Space Telescope Science Institute. These observations are associated with program #6368 and can be accessed via doi: 10.17909/0q3p-sp24.

This research used data obtained with the Dark Energy Spectroscopic Instrument (DESI). DESI construction and operations are managed by the Lawrence Berkeley National Laboratory. This material is based upon work supported by the U.S. Department of Energy, Office of Science, Office of High-Energy Physics, under contract No. DE-AC02-05CH11231 and by the National Energy Research Scientific Computing Center, a DOE Office of Science User Facility under the same contract. Additional support for DESI was provided by the U.S. National Science Foundation (NSF), Division of Astronomical Sciences, under contract No. AST-0950945 to the NSF National Optical-Infrared Astronomy Research Laboratory; the Science and Technology Facilities Council of the United Kingdom; the Gordon and Betty Moore Foundation; the Heising-Simons Foundation; the French Alternative Energies and Atomic Energy Commission (CEA); the National Council of Humanities, Science and Technology of Mexico (CONAHCYT); the Ministry of Science and Innovation of Spain (MICINN); and the DESI Member Institutions (www.desi.lbl.gov/collaborating-institutions). The DESI collaboration is honored to be permitted to conduct scientific research on I'oligam Du'ag (Kitt Peak), a mountain with particular significance to the Tohono O'odham Nation.

M.E.D. thanks Arjun Dey for helpful early comments about the spectrum of CAPERS-LRD-z9. We also acknowledge Haojie Hu for kindly sharing the data from the black hole seeding and growth model, which we use in Figure 5 for comparison with our observational results.

Facility: JWST.

Software: astropy (Astropy Collaboration et al. 2013, 2018, 2022), bagpipes (A. C. Carnall et al. 2018), Cloudy (M. Chatzikos et al. 2023), emcee (D. Foreman-Mackey et al. 2013), JWST pipeline (H. Bushouse et al. 2025), scipy (P. Virtanen et al. 2020), SPARCL (S. Juneau et al. 2024).

Appendix
Flexible Dust Law Fit

Here we describe our fitting procedure and results for a flexible (S. Salim et al. 2018) dust law. We adopt all of the same parameters and procedures described in Section 3.4 with the exception of the AGN component dust here. We substitute the fixed SMC dust law for a flexible slope (S. Salim et al. 2018) dust law. We add the steepness parameter δ to the model parameters and assume a flat prior ranging from $\delta = -5$ to 0. We show the results of this updated fitted model in Figure 8 and Table 3.

The resulting model better reproduces the MIRI F1000W photometry (with residuals $\chi = -0.27$ versus $\chi = -1.8$ with the SMC law). However the best-fit $\delta = -4.66^{+0.31}_{-0.24}$ represents an unphysically steep attenuation curve (see discussion in

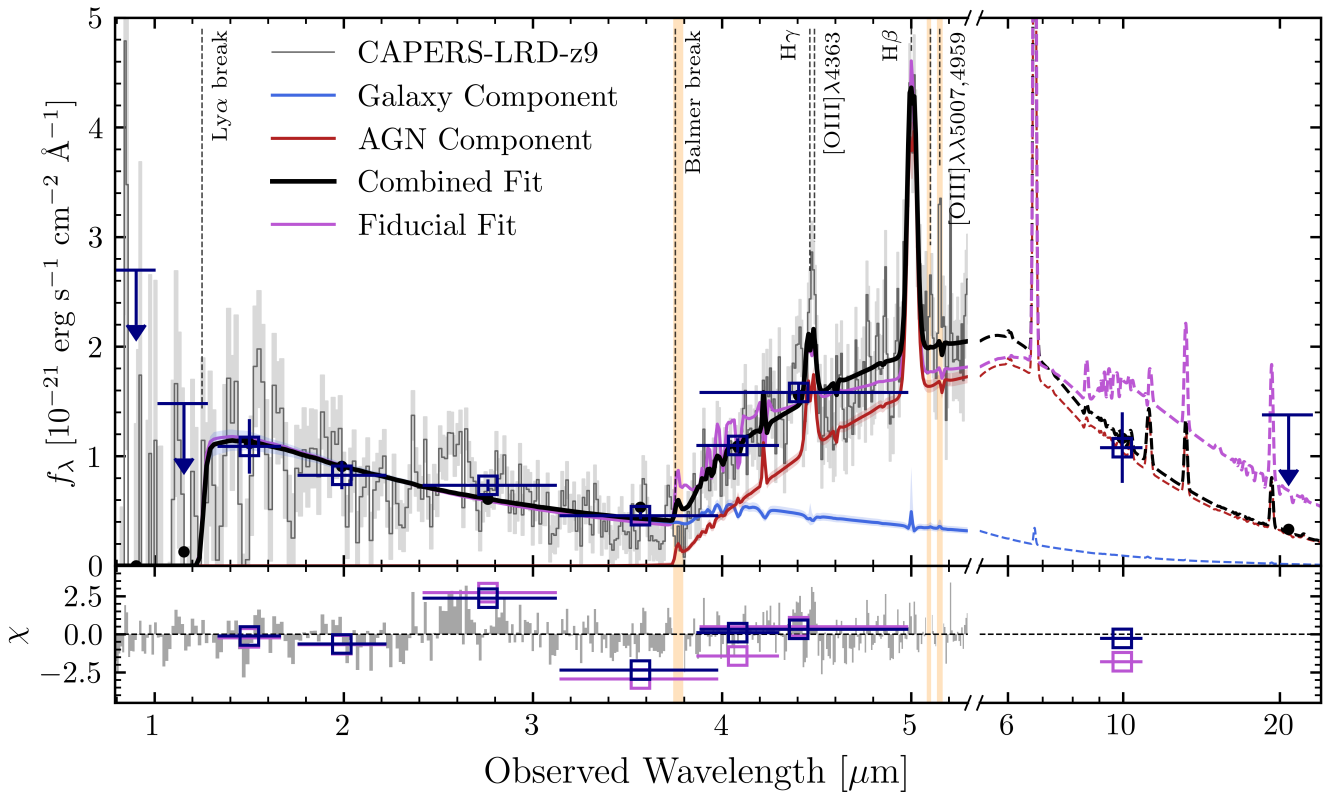

Figure 8. Spectrum and 1σ errors of CAPERS-LRD-z9 (gray curve, light gray shading), the best-fit host galaxy component (solid and dashed blue curves), the best-fit dense-gas-enshrouded AGN component (solid and dashed red curves), combined host+AGN fit (solid and dashed black curves), fiducial SMC dust law fit (solid and dashed purple curves), photometry data (dark blue squares and upper limits), best-fit model photometry (black points) in the upper panel, and masked regions (gold shading). The lower panel shows the χ residuals of the fit for the spectrum (gray curve) and photometry (dark blue squares). Note that the flexible (yet unphysically steep) AGN dust law allows for strong agreement with the MIRI F1000W flux that cannot be reproduced by an SMC law.

Table 3
`Cloudy` Parameter Grid and Fitted Values

Parameter	Grid Values	Fitted Value
$\log T_{\rm BB}$ (K)	4, 4.7, 5, 5.7	5.0
$\alpha_{\rm OX}$	−2.5, −2.0, −1.5	−1.5
$\alpha_{\rm UV}$	−0.1	⋯
$\alpha_{\rm X}$	−0.5	⋯
$\log n_{\rm H}$ (cm^{-3})	9, 9.5, 10, 10.5, 11, 11.5, 12	$10.3^{+0.3}_{-0.3}$
$v_{\rm turb}$ (km s^{-1})	100, 200, 300, 400, 500	134^{+45}_{-26}
[Fe/H]	−2	⋯
$\log U$	−3.5, −3, −2.5, −1.5, −0.5	−1.5
$\log N_{\rm H}$ (cm^{-2})	21, 22, 23, 24, 25, 26	$25.0^{+0.3}_{-0.5}$
C_f	0–1	$0.64^{+0.14}_{-0.13}$
A_V	0–3 (S. Salim et al. 2018 law)	$0.32^{+0.05}_{-0.04}$
δ	−5–0	$-4.66^{+0.31}_{-0.24}$

Note. The first four parameters describe the incident continuum spectrum, where $T_{\rm BB}$ is the "big bump" temperature, $\alpha_{\rm OX}$ is the optical-to-X-ray index, $\alpha_{\rm UV}$ is the power-law UV slope, and $\alpha_{\rm X}$ is the power-law X-ray slope. The incident continuum is passed through dense gas defined by the gas density ($n_{\rm H}$), metallicity ([Fe/H]), and turbulent velocity ($v_{\rm turb}$). The level of irradiation at the face of the cloud is set by the ionization parameter ($\log U$), and the `Cloudy` calculations are stopped at a range of line-of-sight column densities ($N_{\rm H}$). δ is the S. Salim et al. (2018) dust law steepness parameter.

Section 5.2). Clearly, more sophisticated modeling is necessary to reproduce the SEDs of LRDs—including, perhaps, modifications of the intrinsic SED of the AGN accretion disk.

ORCID iDs

Anthony J. Taylor https://orcid.org/0000-0003-1282-7454
Vasily Kokorev https://orcid.org/0000-0002-5588-9156
Dale D. Kocevski https://orcid.org/0000-0002-8360-3880
Hollis B. Akins https://orcid.org/0000-0003-3596-8794
Fergus Cullen https://orcid.org/0000-0002-3736-476X
Mark Dickinson https://orcid.org/0000-0001-5414-5131
Steven L. Finkelstein https://orcid.org/0000-0001-8519-1130
Pablo Arrabal Haro https://orcid.org/0000-0002-7959-8783
Volker Bromm https://orcid.org/0000-0003-0212-2979
Mauro Giavalisco https://orcid.org/0000-0002-7831-8751
Kohei Inayoshi https://orcid.org/0000-0001-9840-4959
Stéphanie Juneau https://orcid.org/0000-0002-0000-2394
Gene C. K. Leung https://orcid.org/0000-0002-9393-6507
Pablo G. Pérez-González https://orcid.org/0000-0003-4528-5639
Rachel S. Somerville https://orcid.org/0000-0002-6748-6821
Jonathan R. Trump https://orcid.org/0000-0002-1410-0470
Ricardo O. Amorín https://orcid.org/0000-0001-5758-1000
Guillermo Barro https://orcid.org/0000-0001-6813-875X
Denis Burgarella https://orcid.org/0000-0002-4193-2539
Madisyn Brooks https://orcid.org/0000-0001-5384-3616
Adam C. Carnall https://orcid.org/0000-0002-1482-5818
Caitlin M. Casey https://orcid.org/0000-0002-0930-6466
Yingjie Cheng https://orcid.org/0000-0001-8551-071X
John Chisholm https://orcid.org/0000-0002-0302-2577

Katherine Chworowsky https://orcid.org/0000-0003-4922-0613
Kelcey Davis https://orcid.org/0000-0001-8047-8351
Callum T. Donnan https://orcid.org/0000-0002-7622-0208
James S. Dunlop https://orcid.org/0000-0002-1404-5950
Richard S. Ellis https://orcid.org/0000-0001-7782-7071
Vital Fernández https://orcid.org/0000-0003-0531-5450
Seiji Fujimoto https://orcid.org/0000-0001-7201-5066
Norman A. Grogin https://orcid.org/0000-0001-9440-8872
Ansh R. Gupta https://orcid.org/0000-0003-4242-8606
Nimish P. Hathi https://orcid.org/0000-0001-6145-5090
Intae Jung https://orcid.org/0000-0003-1187-4240
Michaela Hirschmann https://orcid.org/0000-0002-3301-3321
Jeyhan S. Kartaltepe https://orcid.org/0000-0001-9187-3605
Anton M. Koekemoer https://orcid.org/0000-0002-6610-2048
Rebecca L. Larson https://orcid.org/0000-0003-2366-8858
Ho-Hin Leung https://orcid.org/0000-0003-0486-5178
Mario Llerena https://orcid.org/0000-0003-1354-4296
Ray A. Lucas https://orcid.org/0000-0003-1581-7825
Derek J. McLeod https://orcid.org/0000-0003-4368-3326
Lorenzo Napolitano https://orcid.org/0000-0002-8951-4408
Casey Papovich https://orcid.org/0000-0001-7503-8482
Thomas M. Stanton https://orcid.org/0000-0002-0827-9769
Roberta Tripodi https://orcid.org/0000-0002-9909-3491
Xin Wang https://orcid.org/0000-0002-9373-3865
Stephen M. Wilkins https://orcid.org/0000-0003-3903-6935
L. Y. Aaron Yung https://orcid.org/0000-0003-3466-035X
Jorge A. Zavala https://orcid.org/0000-0002-7051-1100

References

Abuter, R., Allouche, F., Amorim, A., et al. 2024, Natur, 627, 281
Adamo, A., Bradley, L. D., Vanzella, E., et al. 2024, Natur, 632, 513
Agarwal, B., Davis, A. J., Khochfar, S., Natarajan, P., & Dunlop, J. S. 2013, MNRAS, 432, 3438
Akins, H. B., Casey, C. M., Berg, D. A., et al. 2025a, ApJL, 980, L29
Akins, H. B., Casey, C. M., Chisholm, J., et al. 2025b, arXiv:2503.00998
Akins, H. B., Casey, C. M., Lambrides, E., et al. 2024, arXiv:2406.10341
Arrabal Haro, P., Dickinson, M., Finkelstein, S. L., et al. 2023, ApJL, 951, L22
Astropy Collaboration, Price-Whelan, A. M., Lim, P. L., et al. 2022, ApJ, 935, 167
Astropy Collaboration, Price-Whelan, A. M., SipHocz, B. M., et al. 2018, AJ, 156, 123
Astropy Collaboration, Robitaille, T. P., Tollerud, E. J., et al. 2013, A&A, 558, A33
Backhaus, B. E., Bridge, J. S., Trump, J. R., et al. 2023, ApJ, 943, 37
Baggen, J. F. W., van Dokkum, P., Brammer, G., et al. 2024, ApJL, 977, L13
Barro, G., Perez-Gonzalez, P. G., Kocevski, D. D., et al. 2024a, ApJ, 963, 128
Barro, G., Perez-Gonzalez, P. G., Kocevski, D. D., et al. 2024b, arXiv:2412.01887
Barvainis, R. 1987, ApJ, 320, 537
Begelman, M. C., Volonteri, M., & Rees, M. J. 2006, MNRAS, 370, 289
Bentz, M. C., Onken, C. A., Street, R., & Valluri, M. 2023, ApJ, 944, 29
Bentz, M. C., Peterson, B. M., Pogge, R. W., Vestergaard, M., & Onken, C. A. 2006, ApJ, 644, 133
Bhowmick, A. K., Blecha, L., Torrey, P., et al. 2024, MNRAS, 533, 1907
Bogdán, Á., Goulding, A. D., Natarajan, P., et al. 2024, NatAs, 8, 126
Brammer, G. 2022, msaexp: NIRSpec Analyis Tools v0.9.4, Zenodo, doi: 10.5281/zenodo.7299500
Brammer, G. B., van Dokkum, P. G., & Coppi, P. 2008, ApJ, 686, 1503
Brinchmann, J. 2023, MNRAS, 525, 2087
Bromm, V., & Loeb, A. 2003, ApJ, 596, 34
Brooks, M., Simons, R. C., Trump, J. R., et al. 2025, ApJ, 986, 177
Bunker, A. J., Saxena, A., Cameron, A. J., et al. 2023, A&A, 677, A88
Bushouse, H., Eisenhamer, J., Dencheva, N., et al. 2025, JWST Calibration Pipeline v1.18.0, Zenodo, doi:10.5281/zenodo.6984365
Cackett, E. M., Bentz, M. C., & Kara, E. 2021, iSci, 24, 102557
Calzetti, D. 2001, PASP, 113, 1449
Capak, P. L., Carilli, C., Jones, G., et al. 2015, Natur, 522, 455
Carnall, A. C., McLure, R. J., Dunlop, J. S., & Davé, R. 2018, MNRAS, 480, 4379
Carniani, S., Hainline, K., D'Eugenio, F., et al. 2024, Natur, 633, 318
Castellano, M., Fontana, A., Treu, T., et al. 2022, ApJL, 938, L15
Chatzikos, M., Bianchi, S., Camilloni, F., et al. 2023, RMxAA, 59, 327
Chen, C.-H., Ho, L. C., Li, R., & Zhuang, M.-Y. 2025, ApJ, 983, 60
Chon, S., & Omukai, K. 2025, MNRAS, 539, 2561
Cullen, F., Carnall, A. C., Scholte, D., et al. 2025, MNRAS, 540, 2176
de Graaff, A., Rix, H.-W., Naidu, R. P., et al. 2025, arXiv:2503.16600
de Graaff, A. G., Brammer, G., Bezanson, R., et al. 2023, JWST Proposal. Cycle 2, ID. #4233
DESI Collaboration, Abdul-Karim, M., Adame, A. G., et al. 2025, arXiv:2503.14745
Donnan, C. T., McLure, R. J., Dunlop, J. S., et al. 2024, MNRAS, 533, 3222
Du, P., Lu, K.-X., Zhang, Z.-X., et al. 2016, ApJ, 825, 126
Dunlop, J. S., Abraham, R. G., Ashby, M. L. N., et al. 2021, JWST Proposal. Cycle 1, ID. #1837
Fan, X., Bañados, E., & Simcoe, R. A. 2023, ARA&A, 61, 373
Finkelstein, S. L., & Bagley, M. B. 2022, ApJ, 398, 25
Finkelstein, S. L., Bagley, M. B., Arrabal Haro, P., et al. 2022, ApJL, 940, L55
Finkelstein, S. L., Bagley, M. B., Arrabal Haro, P., et al. 2025, ApJL, 983, L4
Finkelstein, S. L., Leung, G. C. K., Bagley, M. B., et al. 2024, ApJL, 969, L2
Fonseca Alvarez, G., Trump, J. R., Homayouni, Y., et al. 2020, ApJ, 899, 73
Foreman-Mackey, D., Hogg, D. W., Lang, D., & Goodman, J. 2013, PASP, 125, 306
Fries, L. B., Trump, J. R., Horne, K., et al. 2024, ApJ, 975, 239
Fujimoto, S., Ouchi, M., Kohno, K., et al. 2024, arXiv:2402.18543
Furtak, L. J., Labbé, I., Zitrin, A., et al. 2024, Natur, 628, 57
Gordon, K. D., Clayton, G. C., Misselt, K. A., Landolt, A. U., & Wolff, M. J. 2003, ApJ, 594, 279
Goulding, A. D., Greene, J. E., Setton, D. J., et al. 2023, ApJL, 955, L24
Greene, J. E., & Ho, L. C. 2005, ApJ, 630, 122
Greene, J. E., Labbe, I., Goulding, A. D., et al. 2024, ApJ, 964, 39
Grogin, N. A., Kocevski, D. D., Faber, S. M., et al. 2011, ApJS, 197, 35
Harikane, Y., Zhang, Y., Nakajima, K., et al. 2023, ApJ, 959, 39
Hopkins, A. M. 2004, ApJ, 615, 209
Horne, K. 1986, PASP, 98, 609
Hu, H., Inayoshi, K., Haiman, Z., Ho, L. C., & Ohsuga, K. 2025, ApJL, 983, L37
Inayoshi, K. 2025, arXiv:2503.05537
Inayoshi, K., & Maiolino, R. 2025, ApJL, 980, L27
Inayoshi, K., Visbal, E., & Haiman, Z. 2020, ARA&A, 58, 27
Isobe, Y., Ouchi, M., Nakajima, K., et al. 2023, ApJ, 956, 139
Jeon, J., Bromm, V., Liu, B., & Finkelstein, S. L. 2025a, ApJ, 979, 127
Jeon, J., Liu, B., Taylor, A. J., et al. 2025b, arXiv:2503.14703
Ji, X., Maiolino, R., Übler, H., et al. 2025, arXiv:2501.13082
Johnson, J. L., & Bromm, V. 2007, MNRAS, 374, 1557
Juneau, S., Jacques, A., Pothier, S., et al. 2024, arXiv:2401.05576
Juodžbalis, I., Ji, X., Maiolino, R., et al. 2024, MNRAS, 535, 853
Juodžbalis, I., Maiolino, R., Baker, W. M., et al. 2025, arXiv:2504.03551
Katz, H., Saxena, A., Cameron, A. J., et al. 2023, MNRAS, 518, 592
Kocevski, D. D., Finkelstein, S. L., Barro, G., et al. 2025, ApJ, 986, 126
Kocevski, D. D., Onoue, M., Inayoshi, K., et al. 2023, ApJL, 954, L4
Koekemoer, A. M., Faber, S. M., Ferguson, H. C., et al. 2011, ApJS, 197, 36
Kokorev, V., Caputi, K. I., Greene, J. E., et al. 2024a, ApJ, 968, 38
Kokorev, V., Chávez Ortiz, Ó. A., Taylor, A. J., et al. 2025, arXiv:2504.12504
Kokorev, V., Chisholm, J., Endsley, R., et al. 2024b, ApJ, 975, 178
Kokorev, V., Fujimoto, S., Labbe, I., et al. 2023, ApJL, 957, L7
Korista, K. T., & Goad, M. R. 2004, ApJ, 606, 749
Kovács, O. E., Bogdán, Á., Natarajan, P., et al. 2024, ApJL, 965, L21
Labbe, I., Greene, J. E., Matthee, J., et al. 2024, arXiv:2412.04557
Labbé, I., van Dokkum, P., Nelson, E., et al. 2023, Natur, 616, 266
Lambrides, E., Garofali, K., Larson, R., et al. 2024, arXiv:2409.13047
Larson, R. L., Finkelstein, S. L., Kocevski, D. D., et al. 2023, ApJL, 953, L29
Lauer, T. R., Tremaine, S., Richstone, D., & Faber, S. M. 2007, ApJ, 670, 249
Leung, G. C. K., Finkelstein, S. L., Pérez-González, P. G., et al. 2024, arXiv:2411.12005
Li, J., Silverman, J. D., & Shen, Y. 2025, ApJ, 981, 19

Lin, X., Fan, X., Wang, F., et al. 2025, arXiv:2504.08039
Liu, B., & Bromm, V. 2022, ApJL, 937, L30
Lupi, A., Trinca, A., Volonteri, M., Dotti, M., & Mazzucchelli, C. 2024, A&A, 689, A128
Luridiana, V., Morisset, C., & Shaw, R. A. 2015, A&A, 573, A42
Lyu, J., & Rieke, G. 2022, Univ, 8, 304
Ma, Y., Greene, J. E., Setton, D. J., et al. 2025, ApJ, 981, 191
Maiolino, R., Risaliti, G., Signorini, M., et al. 2025, MNRAS, 538, 1921
Maiolino, R., Scholtz, J., Curtis-Lake, E., et al. 2024, A&A, 691, A145
Matteri, A., Ferrara, A., & Pallottini, A. 2025, arXiv:2503.18850
Matthee, J., Naidu, R. P., Brammer, G., et al. 2024, ApJ, 963, 129
Mazzolari, G., Übler, H., Maiolino, R., et al. 2024, A&A, 691, A345
Moustakas, J., Scholte, D., Dey, B., & Khederlarian, A. 2023, FastSpecFit, Astrophysics Source Code Library, ascl:2308.005
Mowla, L., Iyer, K., Asada, Y., et al. 2024, Natur, 636, 332
Naidu, R. P., Matthee, J., Katz, H., et al. 2025, arXiv:2503.16596
Naidu, R. P., Oesch, P. A., van Dokkum, P., et al. 2022, ApJL, 940, L14
Napolitano, L., Castellano, M., Pentericci, L., et al. 2024, arXiv:2410.18763
Narayanan, D., Lower, S., Torrey, P., et al. 2024, ApJ, 961, 73
Oke, J. B., & Gunn, J. E. 1983, ApJ, 266, 713
Omukai, K., Schneider, R., & Haiman, Z. 2008, ApJ, 686, 801
Osterbrock, D. E. 1989, Astrophysics of Gaseous Nebulae and Active Galactic Nuclei (Melville, NY: Univ. Science Books)
Östlin, G., Pérez-González, P. G., Melinder, J., et al. 2025, A&A, 696, A57
Pacucci, F., Nguyen, B., Carniani, S., Maiolino, R., & Fan, X. 2023, ApJL, 957, L3
Peng, C. Y., Ho, L. C., Impey, C. D., & Rix, H.-W. 2002, AJ, 124, 266
Pérez-González, P. G., Barro, G., Rieke, G. H., et al. 2024, ApJ, 968, 4
Pérez-González, P. G., Costantin, L., Langeroodi, D., et al. 2023, ApJL, 951, L1
Pérez-González, P. G., Rieke, G. H., Villar, V., et al. 2008, ApJ, 675, 234
Reddy, N. A., Kriek, M., Shapley, A. E., et al. 2015, ApJ, 806, 259
Reddy, N. A., Oesch, P. A., Bouwens, R. J., et al. 2018, ApJ, 853, 56
Regan, J., & Volonteri, M. 2024, OJAp, 7, 72
Robertson, B. E., Tacchella, S., Johnson, B. D., et al. 2023, NatAs, 7, 611
Rusakov, V., Watson, D., Nikopoulos, G. P., et al. 2025, arXiv:2503.16595
Salim, S., Boquien, M., & Lee, J. C. 2018, ApJ, 859, 11
Setton, D. J., Greene, J. E., de Graaff, A., et al. 2024, arXiv:2411.03424
Smith, A., Becerra, F., Bromm, V., & Hernquist, L. 2017, MNRAS, 472, 205
Smith, A., & Bromm, V. 2019, ConPh, 60, 111
Stanway, E. R., & Eldridge, J. J. 2018, MNRAS, 479, 75
Stern, J., & Laor, A. 2012, MNRAS, 423, 600
Storey, P. J., & Zeippen, C. J. 2000, MNRAS, 312, 813
Suh, H., Scharwächter, J., Farina, E. P., et al. 2025, NatAs, 9, 271
Tacchella, S., Johnson, B. D., Robertson, B. E., et al. 2023, MNRAS, 522, 6236
Takeo, E., Inayoshi, K., & Mineshige, S. 2020, MNRAS, 497, 302
Taylor, A. J., Finkelstein, S. L., Kocevski, D. D., et al. 2025, ApJ, 986, 165
Trefoloni, B., Ji, X., Maiolino, R., et al. 2024, arXiv:2410.21867
Trinca, A., Schneider, R., Valiante, R., et al. 2022, MNRAS, 511, 616
Tripodi, R., Martis, N., Markov, V., et al. 2024, arXiv:2412.04983
Übler, H., Maiolino, R., Pérez-González, P. G., et al. 2024, MNRAS, 531, 355
van Hoof, P. A. M. 2018, Galax, 6, 63
Vestergaard, M., & Wilkes, B. J. 2001, ApJS, 134, 1
Virtanen, P., Gommers, R., Oliphant, T. E., et al. 2020, NatMe, 17, 261
Vivian, U., Barth, A. J., Vogler, H. A., et al. 2022, ApJ, 925, 52
Volonteri, M., Habouzit, M., & Colpi, M. 2021, NatRP, 3, 732
Wang, B., de Graaff, A., Davies, R. L., et al. 2025, ApJ, 984, 121
Wang, B., Fujimoto, S., Labbé, I., et al. 2023, ApJL, 957, L34
Wang, B., Leja, J., de Graaff, A., et al. 2024, ApJL, 969, L13
Weibel, A., de Graaff, A., Setton, D. J., et al. 2025, ApJ, 983, 11
Williams, C. C., Alberts, S., Ji, Z., et al. 2024, ApJ, 968, 34
Wise, J. H., Regan, J. A., O'Shea, B. W., et al. 2019, Natur, 566, 85
Woods, T. E., Agarwal, B., Bromm, V., et al. 2019, PASA, 36, e027
Yue, M., Eilers, A.-C., Ananna, T. T., et al. 2024a, ApJL, 974, L26
Yue, M., Eilers, A.-C., Simcoe, R. A., et al. 2024b, ApJ, 966, 176
Zavala, J. A., Castellano, M., Akins, H. B., et al. 2025, NatAs, 9, 155
Zhang, S., Liu, B., Bromm, V., et al. 2025, arXiv:2503.17585
Ziparo, F., Gallerani, S., & Ferrara, A. 2025, JCAP, 2025, 040